Key Points:
- An isotope mixing model was developed to quantify the contributions of rain, ice, and snow meltwater to the total river discharge
- We show heavy monsoonal rainfall triggers the melting of glacier ice resulting in enhanced ice meltwater discharge in streams
- We conclude rainfall events have complex controls on glacial hydrology/processes

Author Contributions:

Conceptualization: Indra S. Sen, Soumita Boral
Data curation: Nita Roy
Formal analysis: Nita Roy, Indra S. Sen
Funding acquisition: Indra S. Sen
Investigation: Nita Roy
Methodology: Nita Roy, Soumita Boral
Project administration: Indra S. Sen
Resources: Indra S. Sen, Soumita Boral, Tanuj Shukla
Software: Nita Roy
Supervision: Indra S. Sen
Validation: Nita Roy
Visualization: Nita Roy, Vinoj Velu
Writing – original draft: Nita Roy
Writing – review & editing: Indra S. Sen

Isotope Hydrograph Separation Reveals Rainfall on the Glaciers Will Enhance Ice Meltwater Discharge to the Himalayan Rivers

Nita Roy[1], Indra S. Sen[1], Soumita Boral[1,2], Tanuj Shukla[1,3], and Vinoj Velu[4]

[1]Department of Earth Sciences, Indian Institute of Technology Kanpur, Kanpur, UP, India, [2]Interdisciplinary Centre for Water Research, Indian Institute of Science Bangalore, Bangalore, Karnataka, India, [3]State Key Laboratory of Cryospheric Science, Northwest Institute of Eco-Environment and Resources, Chinese Academy of Science, Lanzhou, China, [4]School of Earth, Ocean and Climate Sciences, Indian Institute of Technology Bhubaneswar, Bhubaneswar, Odisha, India

Abstract The Indian Summer Monsoon (ISM) and meltwater from the Himalayan are the two most important sources of water in the Indian subcontinent. However, the impact of ISM on Himalayan glaciers and subsequent stream hydrology remains largely unknown. To provide new insight into the impact of rainfall on glacial hydrology, here we present hydro-meteorological and time-series observations of meltwater stable water isotope compositions from the snout of the Chorabari glacier in the Upper Ganga Basin, Central Himalayas across the ablation season corresponding to 2019. We observe that rainfall events (>2 mm d^{-1}) on the glacier enhance discharge driven by ice meltwater in River Mandakini. Energy balance calculations reveal that one of the drivers behind enhanced ice meltwater contribution could be rain-induced melting of the glacier where rainfall on the ice surface melts the glacier producing up to 13% of the total discharge at the glacier snout. Further, rainfall on glacier surface have other control on glacial processes—for example, snow metamorphism, ice flow dynamics such as short-term acceleration in ice speed flow, and reorganization of the englacial and subglacial drainage network—that are poorly studied and needs further investigation. We conclude rainfall events on the glacier have a complex control on mountain hydrology. This study, therefore, provides an interpretative framework that calls for additional assessments of the direct and indirect impact of rainfall in glacial hydrology.

Plain Language Summary Understanding the drivers of elevated ice meltwater runoff in glacier-fed Himalayan streams is critically important in constraining the role of climate change in glacial hydrology. The conventional thinking of elevated ice meltwater runoff in Himalayan rivers is mainly attributed to global warming. However, in this study, we find that rain events on the glacier are an additional driver of enhanced ice meltwater discharge in the glacier-fed Himalayan streams. The additional flux of ice meltwater can be explained by the reorganization of the englacial and subglacial drainage network during rainfall events and/or rain-induced melting of the glacier ice where raindrops falling on the ice surface are releasing sensible and latent heat by englacial cooling and freezing of rain, thereby raising ice temperatures to the melting point, in result, enhanced ice meltwater contributions. As the number of extreme rainfall events and their associated catastrophes has increased in recent decades, the observed causal relationship between ISM and enhanced ice meltwater contributions in the Himalayas is critical to better manage and predict important environmental problems such as floods in the Himalayas.

1. Introduction

The Indian monsoon rainfall and the meltwater runoff from the ice and snow mass stored in the Himalayan and surrounding mountain ranges referred to as the "Third Pole" are the two most important water resources that feed more than a billion people in the Indian Subcontinent (Immerzeel et al., 2010). The annual cycle of the monsoon contains two components (a) the Indian Summer Monsoon (ISM), which originates in the Arabian sea and the Bay of Bengal in July through September (JJAS), and (b) the western disturbances that originate in the Mediterranean Sea in December through March. At present, the south-facing slopes of the Himalayan mountain ranges receive 3,000–4,000 mm yr^{-1} of ISM rainfall which is responsible for 80% of annual rainfall in the Himalayas (Banerjee et al., 2020; Barros et al., 2000; Shekhar et al., 2010; Thayyen et al., 2005). Rain gauge data over ~4,000 m above mean sea level (a.m.s.l.) shows that the glaciated regions in the Himalayas, particularly in the Central Himalayas, can receive 250–700 mm of rainfall per month (Boral et al., 2019).

The rainfall patterns are expected to change in the future. For example, Figure 1 shows that the Central and Western Himalayas record an increasing rainfall trend during the period 1951–2015 due to climate change (Hock et al., 2019). A recent study using 32 global climate models that participated in the latest Coupled Model Intercomparison Project (CMIP6) exercise shows a significant increase in mean rainfall during July through September (JJAS) months in the Himalayan region (Katzenberger et al., 2021). The multi-model mean for JJAS projects an increase in rainfall of 0.33 mm d^{-1} per kelvin of global warming, whereas, the dependence of rainfall on global mean temperature is 5.3% per kelvin of global warming. In addition to increased rainfall projections, a global temperature rise of 1.5°C will lead to a warming of 2.1 ± 0.1°C in the Himalayan and surrounding mountain ranges (Kraaijenbrink et al., 2017). The increase in ISM rainfall in combination with a long-term increase in temperature will result in an increase in the number of wet years and extreme rainfall events that is, torrential precipitation of >100 mm per hour that occurs over a geographical region of ∼25 km^2 in the Himalayas. This is evident as the number of extreme rainfall events in the Himalayas has nearly doubled over the last two decades (Jones et al., 2021; Sharmila et al., 2015; Shukla & Sen, 2021; Turner & Slingo, 2009). As a result, the role of monsoon on the hydrologic cycle of glacierized catchments, landscape evolution, and atmospheric processes has been extensively studied in the Himalayas over the last several decades (Boral & Sen, 2020; Brunello et al., 2020; Hassenruck-Gudipati et al., 2023; Katzenberger et al., 2021; Kraaijenbrink et al., 2017; Maurer et al., 2019; Wang et al., 2020).

However, we have a very limited understanding of the impact of rainfall on the ice and snow mass stored at the "Third Pole." For example, raindrops falling on snow cover (or firn) and ice will release heat by englacial cooling and freezing of rain and thereby raising ice temperatures to the melting point, a process referred to as "rain-induced glacier melting" and in turn, enhancing meltwater runoff in glacier-fed streams (Alexander et al., 2011; Boral et al., 2019; Rai et al., 2019; Reznichenko et al., 2010). In addition to these, rainfall events over glacier surface can modify and reorganize supraglacial, subglacial, and englacial drainage systems resulting in more efficient meltwater transport to the stream (Bartholomew et al., 2011; Benn et al., 2012, 2017; Das et al., 2008; Miles, Steiner, et al., 2017; Miles, Willis, et al., 2017, 2020). As the glacier mass wastage rates in the Himalayas nearly doubled (−0.43 ± 0.14 m w.e. yr^{-1}) in recent years (Maurer et al., 2019), any additional unquantified impact of "rain-induced glacier melting" will have an added adverse effect on the surface mass balance of glacier and changes of the glacial drainage networks. These aspects, which are presently underexplored, are critically important to constrain the interaction of ice- snow-rainwater on the hydrology of the glacierized watersheds made fragile by climate change.

To provide new constraints on the impact of rainfall events on glacier meltwater discharge, we measured stable water isotopes of oxygen and hydrogen (^{18}O/^{16}O and ^{2}H/^{1}H, expressed as δ^{18}O and δD) Mandakini River sampled near the snout of Chorabari Glacier (30°46′20.58″ N; 79°2′59.381″ E, 3553 m a.m.s.l), Upper Ganga basin, Central Himalaya during the entire ablation period between June-to-October (JJASO) of the year 2019. The stable water isotope data and river discharge data were used to develop a hydrograph separation model to determine the contributions of ice meltwater, snow meltwater, and rainwater to the total discharge of the Mandakini River. The hydrograph separation model assumes that river samples are a mixture of water from different source end-members—in this case, ice meltwater, snow meltwater, and rainwater—having distinct geochemical signatures. Stable water isotopes were used to track water source end-member contributions to the discharge because oxygen and hydrogen isotopes get fractionated by natural hydrological processes (Mark & Mckenzie, 2007), and are not significantly affected by biochemical processes (Clark, 2015). In addition, glacial processes like melt-freeze, snow metamorphism, and sublimation-deposition driven by the temperature gradient of the snowpack layer further fractionate the stable water isotopes (Panicker et al., 2019). As a result, water source end-members have unique oxygen and hydrogen isotopic composition (Mark & Mckenzie, 2007) and can be used to construct isotope-based mixing models to track contributions from source end-members that is, ice meltwater, snow meltwater, and rainwater to the total discharge. The weekly time-series relative fractions of ice meltwater, snow meltwater, and rainwater to the total discharge of the Mandakini River was integrated with the measured meteorological data to determine the causal relationship between rainfall, ice meltwater, and snow meltwater discharge in the Mandakini River. Finally, we provide an outlook for future studies related to the direct and indirect impact of rainfall on glacierized catchments of the Himalayas.
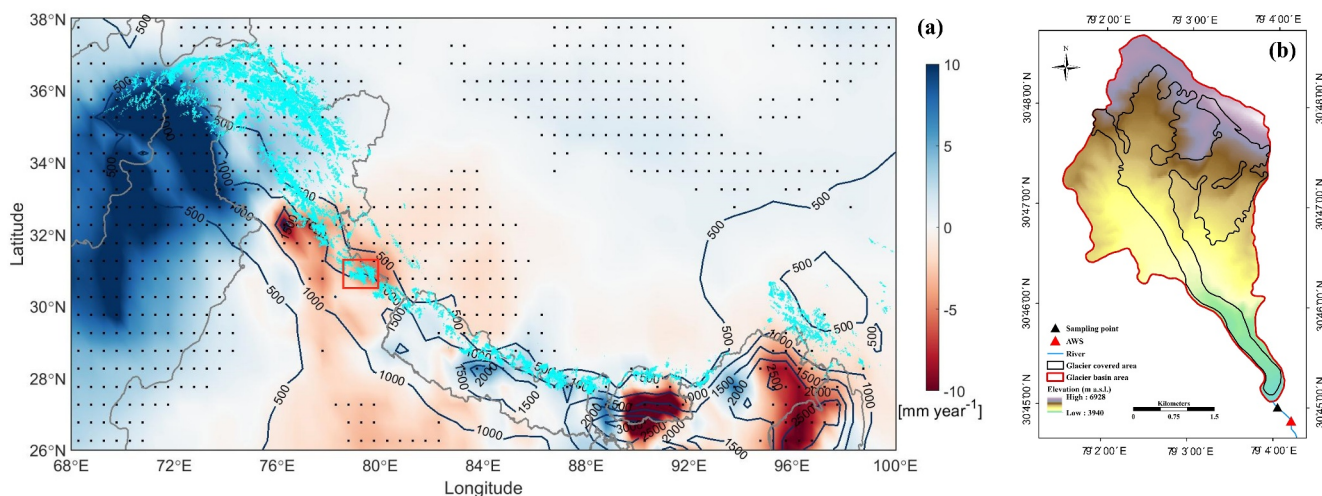
Figure 1. (a) The observed changes in rainfall over the Himalayan region during the period 1951–2015. The color contour shows trends in annual mean rainfall (mm per year), the line contour indicates the climatological mean rainfall (mm). Rainfall data were taken from Aphrodite version-2 APHRO_MA_0.5deg_V1101 (1951–2007) and APHRO_MA_05deg_V1101EX_R1 (2008–2015) (http://aphrodite.st.hirosaki-u.ac.jp/download/, last access: 8 December 2021) at 0.5° resolution in the Asian monsoon region. Black dots are significant at a 95% confidence level. The cyan contours indicate the location of glaciers over the region based on Randolph glacier Inventory 6.0 (Hock et al., 2019). R. Hock et al., "High Mountain Areas" in IPCC Special Report on the Ocean and Cryosphere in a Changing Climate (2019). The red square box shows the location of study area in the Central Himalaya. (b) Catchment area map of Chorabari Glacier with locations of sampling site and Automated Weather station (AWS).

2. Materials and Methods

2.1. Study Area

We used 6-month long (June-to-October) time-series observations near the snout of the Chorabari glacier (30° 46′20.58″ N; 79°2′59.381″ E) located in the Upper Ganga Basin, Central Himalaya, India (Figure 1). Chorabari glacier is a 7.5 km long medium-sized glacier with a catchment area of 15.4 km^2. The glacier flows from north to south ranging in elevation from 6,400 m a.m.s.l. at the head to 3895 m a.m.s.l. at the terminus of the glacier. It is a south facing valley type glacier and has been assigned the specific identification number "IN 50132 02 003" by the Geological Survey of India (Sangewar et al., 2009). River Mandakini originated from the terminus of Chorabari Glacier system near the Kedarnath Temple (30°44′6.72″ N, 79°4′0.84″ E). The Mandakini River flows for 81 km and joins River Alaknanda at Rudraprayag, which flows into the river Ganga. The Chorabari glacier receives summer precipitation from the Indian summer monsoon (ISM) and winter precipitation from Westerlies in the form of snowfall (Kumar et al., 2018).

Chorabari Glacier has a small steep-sloped (30°) accumulation area formed by two cirques, one originating from the Kedarnath peak (6,940 m a.m.s.l) and the other from Bhartkhunta peak (6,578 m a.m.s.l) (Dobhal et al., 2013). The ablation area is gently sloped (10°) and is characterized by crevasses and lateral moraines. The average specific mass balance of the Chorabari glacier was reported to range from −0.82 m w.e. a^{-1} in 2005/06 to −0.67 m w.e. a^{-1} in 2007/08 (Dobhal et al., 2013). It is worth mentioning that a thick debris layer covers ~53% of the total glacier area with debris thickness varying from 5 to >50 cm at different altitudes (Dobhal et al., 2013). Debris cover not only impacts ice melt rates, it also significantly influences the overall mass balance of the Chorabari glacier. The effect of debris cover on ablation rates varies with thickness. Ablation rate reaches its maximum, ranging from 2.3 to 3.3 m yr^{-1} with relatively thin debris cover whereas ablation rate gradually decreases with increasing debris thickness with an ablation rate of 0.75 m yr^{-1} at an altitude of 4,000 m a.s.l. where debris thickness is 53 cm (Dobhal et al., 2013).

The Chorabari glacier belongs to the Pindari formation of the higher Himalayan crystallines (HHC) which is situated north of the Pindari Thrust. The main rock types of the Pindari Formation are comprised of highly metamorphosed banded calc-silicate gneisses and calc-schist rocks interbedded with subordinate biotite-psammitic gneiss and schist (Heim & Gansser, 1939; Karakoti et al., 2017). The Chorabari glacier is mainly dominated by the association of granite-gneiss and migmatites. Dykes and veins of pegmatite and apatite intruded the gneissic rock while small occurrences of carbonates and calc-silicate rocks are also reported.

2.2. Meteorological and Hydrological Data Collection

Meteorological and discharge data were collected during the pre-monsoon (June), monsoon (July–August) and post-monsoon (September–mid October) throughout the entire ablation season (JJASO) of the year 2019. We were unable to complete a year-long data collection since this site remains inaccessible from November to May. The meteorological parameters namely air temperature, wind speed, wind direction, atmospheric pressure, relative humidity, dew point, and precipitation data were measured using an Automated Weather Station (AWS) installed ∼300 m below the glacier terminus at an elevation of ∼3,553 m a.m.s.l. The meteorological parameters were recorded manually daily at an interval of 4 hr between 8.30 and 20.30 hr. This measurement interval was chosen based on logistical constraints as the AWS was not equipped with a data logger.

Discharge of the River Mandakini was measured 200 m downstream of the glacier snout using the velocity-area method (Kumar et al., 2014) on daily scale. The discharge site was selected in a stable part of the stream, where the rate of erosion and deposition was visually less so that the cross-sectional area of the river was comparatively uniform throughout the ablation season, and river flow was relatively calm and non-turbulent. The gauging site was prepared using rocks and sandbags along the stream banks to channel the streamflow. A manual staff gauge was installed in the river cross-section to record water levels, coinciding approximately with its minimum level around 9:00 and maximum level around 17:00 hr on a daily basis.

Cross-section of the stream was established from water depth recorded at equal intervals across the channel at the beginning of the ablation season and was rechecked at the end of the season. The Surface velocity of the stream was measured by recording the travel time of a wooden float over a distance of 10 m. The measurement was done three times to reduce manual error, and the mean value of the three recorded travel times was used (Kumar et al., 2016, 2018). We acknowledge that the measurement of velocity with the floating wood method has its own limitations, but this was the only way to measure discharge in a safe manner. Please note that these streams are extremely turbulent and since the streams change their courses very frequently, building a discharge site at a single location was not a wise approach. The uncertainty associated with discharge measurement results in uncertainties regarding the various components of meltwater discharge. However, our objectives were not to quantify the flow components of the discharge, but rather to look at processes. We argue that the use of the floating wood to measure discharge is justified to track trends, and even if it has uncertainties, will not have a substantial bearing on the findings of this study. The mean flow velocity of the Mandakini River was calculated using a reduction co-efficient (0.85) commonly used for Himalayan streams (Bhutiyani, 2000; Kumar et al., 2018; Østrem, 1964). The Mandakini stream discharge was calculated according to the equations

$$V_s = D/T_m \tag{1}$$

$$V_m = 0.85 \times V_s \tag{2}$$

$$Q = A \times V_m \tag{3}$$

where V_s is the surface velocity of the stream (m s^{-1}), D is the 10-m distance the wooden float traveled, T_m is the travel times (second), V_m is the mean flow velocity of the stream (m s^{-1}), Q is the proglacial stream discharge (m^3 s^{-1}) and A is the cross-sectional area of the stream (m^2). The average coefficients of variation (%CV) associated with discharge measurement using area-velocity method are 3% for both daytime and nighttime samples.

2.3. Sample Collection

River water samples ($n = 78$) were collected from the gauging site 200 m downstream of the snout of the Chorabari glacier. Water samples were collected at 9.00 and 17:00 hr at 2 days interval throughout the entire ablation season (JJASO) of the year 2019. Water samples were collected concurrently with discharge measurement. Samples collected at 17:00 hr that is, daytime samples, whereas, samples collected at 9:00 hr are nighttime samples. We collected the samples during daytime and nighttime to capture the diurnal variability of the various flow components. Rainwater samples ($n = 27$) were collected soon after a rain event from manual rain gauge in order to avoid the isotopic fractionation due to atmospheric exchange process of the samples.

The river water and rainwater samples were collected in pre-cleaned high-density polyethylene (HDPE) 1 L bottle and were immediately filtered through Tarson vacuum filtration unit using a 0.22 µm Millipore polyethersulfone (PES) membranes. Filtered water was transferred into a 4 ml amber glass vial with no head-space for oxygen and hydrogen isotope measurements. In addition to river water and rainwater, snow samples ($n = 3$) were collected from winter snowpack at three locations: S1 (30°49′46.3″ N, 79°03′40.3″ E; 3,862 m a.m.s.l.), S2 (30°44′58″ N, 79°03′52.8″ E; 3,920 m a.m.s.l.), and S3 (30°45′28.9″ N, 79°03′31.2″ E; 4,028 m a.m.s.l.) in the month of June 2019. Snow samples were collected from the top layer (10–15 cm) of winter snowpack using a shovel. Similarly, ice samples ($n = 6$) were collected from vertical sections of exposed ice wall near the snout of the glacier at three locations: G1 (30°45′19.1″ N, 79°03′40.1″ E, 3,973 m a.m.s.l.), G2 (30°45′20.1″ N, 79°03′32.5″ E, 4,019 m a.m.s.l.), and G3 (30°45′29″ N, 79°03′29.7″ E, 4,060 m a.m.s.l.). The samples of snow and ice were kept inside pre-cleaned plastic zip-lock bags, upon melting the samples were transferred into 4 mL amber glass vials for oxygen and hydrogen isotope analysis. The pre-cleaning of HDPE bottles and zip-lock bags was done using 10% hydrochloric (HCl) acids (Reagent grade, Fisher scientific), gravimetrically diluted from trace metal grade concentrated HCl acids purified from reagent grade acids in the CUPOLA STILL closed sub-boiling distillation system from PicTrace GmbH, Germany. Physico-chemical parameter namely electrical conductivity (EC) of river water, rain samples, snow and ice meltwater were measured with a portable HI991301 pH/EC/TDS Meter.

2.4. Sample Analysis and Data Quality

Oxygen and hydrogen isotopes of water (river, rain, snow, and ice) were determined by isotope ratio infrared spectroscopy based on off-axis integrated cavity output spectroscopy (Los Gatos Research; LGR) at the Department of Earth Sciences, Indian Institute of Technology Kanpur. The isotope ratios of oxygen and hydrogen are reported using the standard δ notation ($\delta^{18}O$ (‰) = [$(^{18}O/^{16}O)_{sample}/(^{18}O/^{16}O)_{VSMOW} - 1$] × 1,000; δD (‰) = [$(^{2}H/^{1}H)_{sample}/(^{2}H/^{1}H)_{VSMOW} - 1$] × 100 in per mil relative to Vienna Standard Mean Ocean Water (VSMOW). Briefly, about 1 mL of water was kept in vials placed into 54-position trays on the auto-injector tray holder. Water samples were injected through a 1.2 µl syringe in the auto-injector into a heated port kept at ∼90°C via. silicone septum. Vapourization of injected water samples occurred in the heated port and the vapors were introduced into the optical cavity evacuated with a diaphragm pump through a PTFE transfer tube. Each sample was injected 6 times, and the first two results were discarded to eliminate instrumental memory effects. To assess the data quality, Vienna Standard Mean Ocean Water (VSMOW), Standard Light Antarctic Precipitation (SLAP), and Greenland Ice Sheet Precipitation (GISP) were analyzed in bracket sets of five samples, with standard calibration corrections. In addition, reference materials provided by Los Gatos Research (LGR-3C and LGR-5C) were also analyzed. Deuterium excess ($d = \delta D - 8 \times \delta^{18}O$) was calculated following Dansgaard (1964).

The measured values for each standard along with their standard deviations were: VSMOW: $\delta D = 0.4 \pm 0.1‰$ and $\delta^{18}O = 0.1 \pm 0.1‰$; SLAP: $\delta D = -427.2 \pm 0.1‰$ and $\delta^{18}O = -55.37 \pm 0.03‰$ ($n = 90$); GISP: $\delta D = -189.7 \pm 0.3‰$ and $\delta^{18}O = -24.83 \pm 0.11‰$ ($n = 90$); LGR-3C: $\delta D = 97.5 \pm 0.1‰$ and $\delta^{18}O = -13.5 \pm 0.04‰$ ($n = 90$); LGR-5C: $\delta D = -9.1‰$ and $\delta^{18}O = -2.7 \pm 0.1‰$ ($n = 90$). The certified values for each standard are as follows: VSMOW: $\delta D = 0.00‰$ and $\delta^{18}O = 0.00‰$; SLAP: $\delta D = -427.5‰$, and $\delta^{18}O = -55.5‰$; GISP: $\delta D = -189.5‰$ and $\delta^{18}O = -24.76‰$; LGR-3C: $\delta D = 97.3‰$ and $\delta^{18}O = -13.39‰$; LGR-5C: $\delta D = -9.2‰$ and $\delta^{18}O = -2.69‰$. The overall accuracy or reproducibility of the measurements of all reference standards were <0.6‰ for δD and <0.3‰ for $\delta^{18}O$, with a precision better than 0.2‰ for δD and 0.1‰ for $\delta^{18}O$.

2.5. The Choice of Tracers and Assumption in Hydrograph Separation Model

A dual tracer ($\delta^{18}O$ and d values) mixing model was used to quantify the sources of water (hereafter referred to as "water source end-members"). In this study, we used d values over δD as $\delta^{18}O$ and δD showed a strong correlation and could not be treated as independent tracers (Figures 2a and 2b), whereas, $\delta^{18}O$ and d values did not significantly covary (Figures 3a and 3b) and could be treated as independent tracers. The mixing model assumes that (a) the river water is composed of snow meltwater (subscript "s"), rainwater (subscript "r"), and ice meltwater (subscript "i"); (b) we neglect contributions from water source end-members such as mountainous groundwater system and hyporheic zone water to the total flow and; (c) $\delta^{18}O$ and d values of river water represent contributions from water source end-members, and secondary processes such as evaporation did not significantly alter the isotopic composition of the river water, which is evident on the $\delta^{18}O$ versus δD plot (Figure 2). Neglecting groundwater contributions to the total flow is justified because (a) we sampled river
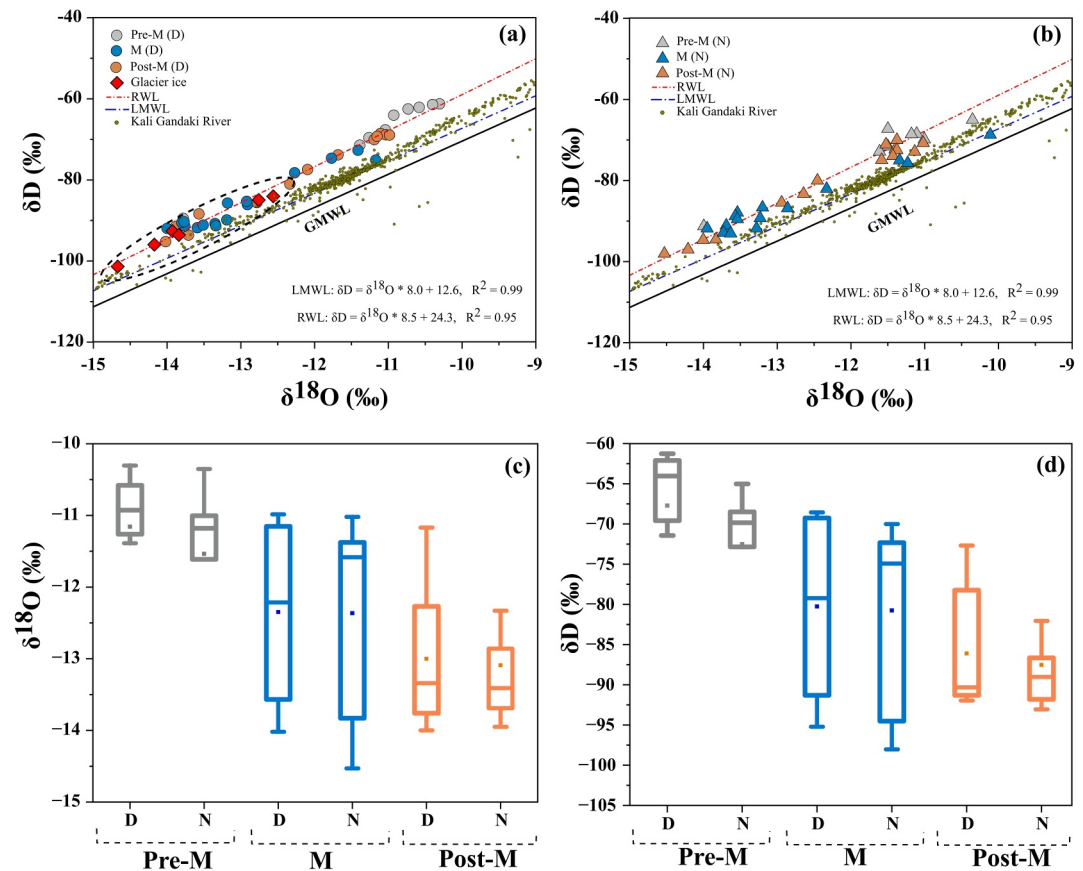
Figure 2. The $\delta^{18}O$ and δD composition of river water and ice samples: (a) daytime and (b) nighttime river water samples, collected in 2019. The dotted area represents isotopic range of ice samples. Samples from Kali Gandaki river (Hassenruck-Gudipati et al., 2023) are also plotted for comparison. Box-and –whisker plot of (c) $\delta^{18}O$ and (d) δD composition of river water showing seasonal and diurnal variability. The Global Meteoric Water Line [$\delta D = \delta^{18}O \times 8.17 + 11.27$ (Rozanski et al., 2013)] and Local Meteoric Water Line along with the best fit River Water Line (RWL) are plotted for comparison. Gray, blue, and orange represent Pre-M, M, and Post-M seasons respectively. Abbreviations: Pre-M (pre-monsoon), M (monsoon), Post-M (post-monsoon), D (daytime samples), N (nighttime samples), GMWL (Global Meteoric Water Line), LMWL (Local Meteoric Water Line), RWL (River Water Line).

water near the snout of the glacier—that is, 200 m from the glacier snout—and therefore the most dominant flows have to be ice meltwater, snow meltwater, and rainwater runoffs (b) the bedrock geology consists of crystalline rocks and we don't have any evidence of thick aquifers in the study region and (c) if groundwater contribution was substantial to the total flow, we should expect a higher Cl^- concentration than what we found in the studied river water (5–25 µmol L^{-1}, Roy & Sen, 2023). Moreover, the studied catchment is steep and covered with a thick debris cover made of gneissic crystalline rocks. Even if we consider that rain falls over the thick debris, given the slope of the ablation zone (10°), it will flow as direct runoff through the base of the glacier and is unlikely to percolate through crystalline rocks. If a small fraction of the flow travels through cracks in the crystalline basement, it is likely that they will be frozen as we are looking at an elevation >3,800 m a.m.s.l. Therefore, any ground seepage will be meltwater only.

We would further like to mention that we chose not to use other tracers such as temperature-compensated electrical conductivity (EC) values—the most commonly used tracer for hydrograph separation (Frenierre & Mark, 2014; Maurya et al., 2011; Rai et al., 2019) in this study because the assumption that EC or most of the other chemical tracers are conservative may not be valid. For example, the temperature-compensated EC concentrations of ice and snow meltwater ranged between 6 to 12 µs cm^{-1} and 3 to 7 µs cm^{-1} (Table S1 in Supporting Information S2), respectively. Whereas, the river water samples had a temperature-compensated EC value in the range of 36 to 92 µs cm^{-1} (Table 1), which is much higher than the source end-members. Groundwater on the other hand has a much higher EC value due to prolonged water-rock interactions in aquifers. For example, Maurya
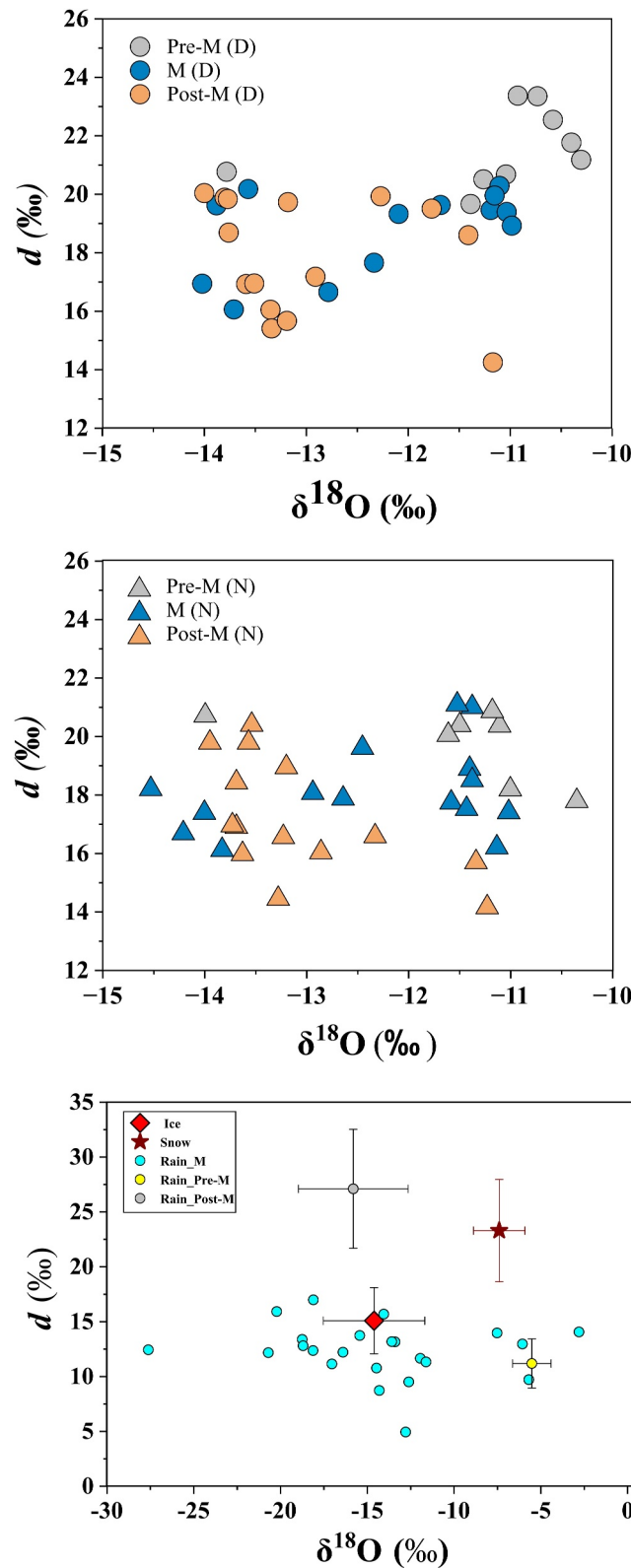
Figure 3. Seasonal variation of $\delta^{18}O$ and d-excess composition of river water for (a) daytime and (b) nighttime samples and (c) end members: rain water, snow and ice samples. Data points with red outline are average composition of snow and ice end members. Average data of rain for pre monsoon and post monsoon period and snow samples are taken from Kumar et al. (2018). Average data of ice sample are combined data of our data and literature data (Table S1 in Supporting Information S2). Rain data for monsoon are from our study collected during 2019 (Table S4 in Supporting Information S2).

Table 1
Time Series Data of δ¹⁸O, δD and d (D-Excess) of River Water Samples Collected From the Snout of Chorabari Glacier in 2019 Along With the Calculated Mean and One Standard Deviation (1σ) of Volumetric Contributions ($m^3 s^{-1}$) of Ice Meltwater, Rainwater and Snow Meltwater From the δ¹⁸O-d Model

Date	δD (‰)	δ¹⁸O (‰)	d (‰)	EC μs cm⁻¹	Mean air T (°C)	Q ($m^3 s^{-1}$)	Ice meltwater Mean	1σ	Rainwater Mean	1σ	Snow meltwater Mean	1σ
Daytime												
02-June-19	−61.25	−10.3	21.18	56	10.00	3.8	1.38	0.30	0.27	0.19	2.15	0.30
05-June-19	−61.43	−10.4	21.77	44	15.67	5.32	1.87	0.38	0.3	0.22	3.15	0.37
08-June-19	−62.1	−10.58	22.55	85	11.50	4.57	1.55	0.28	0.18	0.14	2.84	0.27
14-June-19	−64.04	−10.93	23.37	41	14.50	5.18	1.71	0.22	0.12	0.1	3.34	0.21
17-June-19	−69.59	−11.26	20.51	62	10.25	4.41	2.02	0.34	0.27	0.2	2.12	0.33
20-June-19	−67.65	−11.04	20.68	71	11.50	4.91	2.13	0.37	0.31	0.22	2.47	0.37
23-June-19	−62.5	−10.73	23.35	76	14.00	5.15	1.63	0.24	0.14	0.11	3.38	0.24
26-June-19	−71.43	−11.39	19.67	72	10.00	5.39	2.66	0.46	0.4	0.28	2.33	0.46
29-June-19	−89.47	−13.78	20.77	65	6.13	4.94	3.15	0.15	0.08	0.06	1.7	0.14
08-July-19	−70.07	−11.19	19.46	49	6.36	6.13	3.14	0.54	0.51	0.35	2.47	0.6
14-July-19	−68.56	−11.11	20.28	43	7.09	7.09	3.09	0.58	0.7	0.47	3.3	0.58
17-July-19	−68.88	−11.03	19.39	48	10.00	8.04	3.8	0.77	0.67	0.45	3.57	0.75
20-July-19	−69.26	−11.15	19.96	54	12.00	7.25	3.56	0.59	0.53	0.37	3.16	0.65
23-July-19	−68.94	−10.98	18.93	46	15.00	9.56	4.96	0.95	0.97	0.63	3.63	1.05
29-July-19	−73.83	−11.68	19.63	50	13.25	10.03	5.4	0.8	0.68	0.48	3.96	0.9
01-August-19	−77.43	−12.09	19.33	36	11.50	10.91	5.34	1.07	1.22	0.83	4.35	0.81
07-August-19	−81.02	−12.34	17.66	58	11.67	10.78	4.76	2.17	2.24	1.27	3.78	1.3
10-August-19	−85.61	−12.78	16.66	59	13.00	10.83	5.91	2.18	1.13	0.7	3.8	1.66
13-August-19	−88.37	−13.57	20.18	41	12.75	11.52	6.42	0.99	1.11	0.82	3.99	0.46
19-August-19	−91.31	−13.34	15.41	85	10.00	11.87	8.14	1.67	1.1	0.63	2.63	1.31
22-August-19	−93.62	−13.71	16.06	54	10.50	11.77	7.07	2.09	1.47	0.79	3.23	1.55
25-August-19	−95.22	−14.02	16.94	60	11.00	10.19	7.03	1.06	1.25	0.77	1.91	0.79
28-August-19	−91.42	−13.88	19.62	68	13.50	9.51	6.23	0.54	0.43	0.32	2.85	0.42
03-September-19	−91.39	−13.76	18.69	37	12.67	9.81	5.99	1.17	2.01	1.18	1.8	1.01
06-September-19	−90.75	−13.35	16.05	41	16.33	9.12	6.84	0.85	0.91	0.67	1.37	0.95
09-September-19	−90.52	−13.8	19.88	49	13.00	6.67	3.47	0.86	1.91	0.91	1.29	0.68
12-September-19	−91.31	−13.34	15.41	38	17.00	6.04	4.77	0.5	0.49	0.37	0.77	0.57
15-September-19	−86.1	−12.91	17.18	46	17.50	6.64	4.48	0.75	0.81	0.56	1.34	0.8
18-September-19	−85.71	−13.18	19.73	84	14.00	5.75	2.98	0.74	1.41	0.74	1.36	0.66
21-September-19	−89.85	−13.19	15.67	78	14.50	5.43	4.19	0.48	0.47	0.35	0.77	0.55
24-September-19	−78.23	−12.27	19.93	53	11.50	5.64	2.62	0.76	1.17	0.66	1.84	0.7
27-September-19	−90.32	−13.77	19.84	79	11.00	5.4	2.81	0.7	1.52	0.73	1.06	0.55
30-September-19	−91.79	−13.59	16.93	90	9.50	4.37	3.08	0.44	0.57	0.39	0.73	0.46
03-September-19	−91.96	−14	20.04	114	4.50	3.7	1.89	0.48	1.14	0.51	0.67	0.36
06-September-19	−75.11	−11.17	14.25	85	5.00	2.73	2.2	0.12	0.05	0.04	0.48	0.12
09-September-19	−74.65	−11.77	19.51	110	6.00	2.63	1.23	0.36	0.42	0.26	0.97	0.32
12-September-19	−72.68	−11.41	18.6	85	6.00	2.44	1.24	0.33	0.26	0.18	0.94	0.31
15-September-19	−91.13	−13.51	16.95	118	7.00	2.24	1.57	0.23	0.29	0.2	0.39	0.24

Table 1
Continued

Date	δD (‰)	δ^{18}O (‰)	d (‰)	EC μs cm^{-1}	Mean air T (°C)	Q (m^3 s^{-1})	Ice meltwater Mean	1σ	Rainwater Mean	1σ	Snow meltwater Mean	1σ
Nighttime												
02-June-19	−65.02	−10.35	17.79	72	10.00	3.64	1.64	0.39	0.59	0.32	1.4	0.42
05-June-19	−68.5	−11.11	20.37	66	15.67	4.77	2.14	0.38	0.33	0.23	2.3	0.38
14-June-19	−68.57	−11.18	20.87	58	14.50	4.57	2	0.32	0.26	0.19	2.31	0.33
17-June-19	−71.6	−11.5	20.39	87	10.25	4.05	1.95	0.3	0.24	0.17	1.87	0.3
20-June-19	−72.84	−11.61	20.05	61	11.50	4.57	2.27	0.35	0.29	0.2	2.02	0.36
26-June-19	−69.84	−11	18.19	65	10.00	4.79	2.44	0.54	0.59	0.37	1.76	0.53
29-June-19	−91.24	−14	20.72	60	14.00	4.7	3.08	0.13	0.07	0.05	1.55	0.12
08-July-19	−72.32	−11.4	18.9	42	6.13	5.8	3.2	0.55	0.53	0.36	2.08	0.61
11-July-19	−72.88	−11.14	16.21	40	6.36	5.93	3.34	0.73	1.1	0.54	1.49	0.67
14-July-19	−70.01	−11.38	21.01	38	7.09	5.82	2.55	0.4	0.41	0.29	2.86	0.4
17-July-19	−70.74	−11.02	17.41	49	10.00	7.82	4.12	0.92	1.09	0.62	2.62	0.88
20-July-19	−71.1	−11.52	21.09	56	12.00	6.19	2.92	0.39	0.28	0.21	2.98	0.42
23-July-19	−72.51	−11.38	18.51	83	15.00	5.95	3.37	0.62	0.6	0.4	1.98	0.67
29-July-19	−74.93	−11.58	17.74	54	13.25	8.97	5.51	1.02	1.07	0.67	2.39	1.09
01-August-19	−73.93	−11.43	17.52	48	11.50	10.35	4.27	1.57	2.41	1.33	3.67	1.03
07-August-19	−80.02	−12.45	19.61	58	11.67	10.48	3.04	1.75	2.98	1.3	4.46	0.85
10-August-19	−85.45	−12.94	18.07	46	13.00	10.41	4.55	2.21	1.4	0.76	4.47	1.61
13-August-19	−83.27	−12.64	17.88	53	12.75	11.09	3.37	2.28	4.03	2.07	3.68	0.83
19-August-19	−94.52	−13.83	16.12	56	10.00	11.49	6.77	2.13	1.52	0.82	3.2	1.55
22-August-19	−94.64	−14	17.39	61	10.50	11.13	5.21	2.41	1.9	0.91	4.02	1.69
28-August-19	−96.99	−14.21	16.69	61	13.50	8.98	6.31	0.9	1.17	0.69	1.5	0.67
31-August-19	−98.04	−14.53	18.2	50	13.67	9.21	6.84	0.69	0.56	0.41	1.81	0.53
03-September-19	−91.81	−13.95	19.79	53	12.67	7.9	4.17	1.01	2.29	1.06	1.44	0.78
06-September-19	−92.61	−13.69	16.91	60	16.33	8.67	6.12	0.86	1.12	0.77	1.43	0.89
09-September-19	−91.09	−13.69	18.43	58	13.00	6.14	3.84	0.73	1.16	0.71	1.14	0.65
12-September-19	−89.28	−13.23	16.56	71	17.00	5.8	4.16	0.59	0.65	0.46	0.99	0.65
15-September-19	−87.92	−13.54	20.4	58	17.50	5.87	2.76	0.79	1.83	0.82	1.28	0.63
18-September-19	−86.65	−13.2	18.95	78	14.00	5.47	3.16	0.68	1.1	0.64	1.22	0.63
21-September-19	−92.88	−13.73	16.96	80	14.50	4.8	3.39	0.47	0.63	0.43	0.78	0.49
24-September-19	−86.84	−12.86	16.04	77	11.50	5.18	3.85	0.5	0.48	0.35	0.84	0.57
27-September-19	−82.05	−12.33	16.59	74	11.00	5.82	4.08	0.66	0.54	0.39	1.19	0.72
30-September-19	−91.79	−13.28	14.45	89	9.50	4.08	3.49	0.24	0.24	0.18	0.35	0.27
03-October-19	−93.06	−13.63	15.98	117	4.50	3.7	2.79	0.33	0.37	0.27	0.54	0.37
06-October-19	−75.02	−11.34	15.7	90	5.00	2.83	2.03	0.24	0.12	0.1	0.68	0.25
09-October-19	−75.68	−11.23	14.16	109	6.00	2.6	2.12	0.11	0.05	0.04	0.43	0.11
15-October-19	−88.77	−13.57	19.79	118	7.00	2.22	1.15	0.28	0.60	0.30	0.46	0.24

et al. (2011) reported the EC of groundwater of 340 μs cm^{-1} from Devprayag (the confluence point of River Alaknanda and River Bhagirathi). Since the groundwater contributions to the total flow are minimal, the observed EC values in the range of 36–92 (μs cm^{-1}) are because the snow and ice meltwater interacted with the bedrock and soil, and with the glacial flour in the turbulent streams or flushing events. Therefore, the assumption that the EC behaved in a conservative fashion from source to sink may not be valid.

2.5.1. δ^{18}O and d Mixing Model

The steady-state mass balance Equations 4–6 were solved to obtain the different proportions of water source end members (Klaus & McDonnell, 2013; Penna, 2019; Phillips & Gregg, 2003).

$$f_i \, \delta^{18}O_i + f_s \, \delta^{18}O_s + f_r \, \delta^{18}O_r = \delta^{18}O_{river} \tag{4}$$

$$f_i \, d_i + f_s \, d_s + f_r \, d_r = d_{river} \tag{5}$$

$$f_i + f_s + f_r = 1 \tag{6}$$

where $\delta^{18}O_{river}$ and d_{river} are measured compositions of river water; $\delta^{18}O_i$ and d_i are the compositions of ice meltwater; $\delta^{18}O_s$ and d_s are the compositions of snow meltwater; $\delta^{18}O_r$ and d_r are the compositions of rainwater; and f_i, f_s, f_r are the fractional contributions of ice meltwater, snow meltwater, and rainwater. The vector form of the above equations is

$$\begin{bmatrix} 1 & 1 & 1 \\ \delta^{18}O_i & \delta^{18}O_s & \delta^{18}O_r \\ d_i & d_s & d_r \end{bmatrix} \begin{bmatrix} f_i \\ f_s \\ f_r \end{bmatrix} = \begin{bmatrix} 1 \\ \delta^{18}O_{river} \\ d_{river} \end{bmatrix} \tag{7}$$

$$\text{Which can be written as } A \times f = B \tag{8}$$

Where

$$A = \begin{bmatrix} 1 & 1 & 1 \\ \delta^{18}i & \delta^{18}O_s & \delta^{18}O_r \\ d_i & d_s & d_r \end{bmatrix} \tag{9}$$

$$f = \begin{bmatrix} f_i \\ f_s \\ f_r \end{bmatrix} \tag{10}$$

And

$$B = \begin{bmatrix} 1 \\ \delta^{18}O_{river} \\ d_{river} \end{bmatrix} \tag{11}$$

By dividing the right side of Equation 8 we obtain $f = B \times A^{-1}$ that is,

$$\begin{bmatrix} f_i \\ f_s \\ f_r \end{bmatrix} = \begin{bmatrix} 1 \\ \delta^{18}O_{river} \\ d_{river} \end{bmatrix} \begin{bmatrix} 1 & 1 & 1 \\ \delta^{18}O_i & \delta^{18}O_s & \delta^{18}O_r \\ d_i & d_s & d_r \end{bmatrix}^{-1} \tag{12}$$

Equation 12 was solved for "f" to estimate different end member fractions.

2.5.2. Mixing Model Input Parameters

The two-input parameters in the mixing model were (a) measured $\delta^{18}O$ and d values of river water, and (b) $\delta^{18}O$ and d values of three water source end-members that is, ice meltwater, snow meltwater, and rainwater. Quantifying the source end-member compositions of ice meltwater, snow meltwater, and rainwater is a challenging task because of large natural variability (Ahluwalia et al., 2016; Boral et al., 2019; Lee et al., 2010; Pu et al., 2020; Rai et al., 2013). In this study, we have combined our own data with the available data set of the region to assign the best possible source end-member $\delta^{18}O$ and d-value compositions. Such compilation is valid as the region has the same moisture source that is, derived from ISM and Western Disturbances. Also, ice melting is not an individual season-specific phenomenon as ice is made of snow that gets compressed over many years. Therefore, we combined our data set with literature data sets to capture the natural variability, both in space and time, to provide more realistic source end-member compositions. The end-member compositions have been listed in Table 2. Since end-member $\delta^{18}O$ and d values show large variability, we assigned ±20% relative variation to the average value to capture the variability and assign a possible compositional range, instead of using a unique value, as has been done in previous studies (Kumar et al., 2020; Rai et al., 2019; Singh et al., 2019).

The $\delta^{18}O$ and d values of ice end-member were −14.61 and 15.08‰, respectively (combining literature data and our data, Supplementary Information Table S1). However, end member values of snow sample and pre-monsoon and post-monsoon rain data are taken from other literature (see Table 2 for more details). For snow $\delta^{18}O$ and d end-member values, data were collected from Dokriani glacier (3,965–6,200 m a.s.l.), which is in close proximity to Chorabari glacier. For snow end-member, we used average $\delta^{18}O = -7.4‰$ and $d = 23.3‰$ ($n = 45$) (Kumar et al., 2018). For rainwater composition, we used season-specific and event-specific rain compositions. As June (total rainfall 62 mm) and September (total rainfall 63 mm) did not receive heavy rainfall and river water samples were mostly collected on rain-free days, average rain data for June and September were chosen from Kumar et al. (2018) ($\delta^{18}O = -5.52‰$ and $d = 11.19‰$ for June and $\delta^{18}O = -15.81‰$ and $d = 27.11‰$ for September). On contrary, the monsoon months that is, July and August received 129 and 393 mm of rainfall, respectively, in 2019. Therefore, for July and August, we used $\delta^{18}O$ and d values of major rain events that occurred on or close to the sampling date. Briefly, 11 major rainfall events were identified based on rainfall duration and intensity. The events had a rainfall rate of a minimum of 2 mm d^{-1} and were separated by a dry period no longer than 4 hr before river water sample collection and discharge measurement. It is worth mentioning that the Mandakini River water was sampled along with the rainfall events. Since the isotopic composition of rain during an intra-event can vary from 1‰ to 5‰ (Han et al., 2020), we assigned ±5% variability for event-specific rain events to obtain a possible compositional range (Table 2). The end-member compositional ranges used in $\delta^{18}O$-d mixing model were chosen in such a way that the river water samples fall within the space enclosed by the end-member values (Figure S1 in Supporting Information S1).

2.5.3. Mixing Model Execution and Uncertainty Analysis

Equation 9 was solved to obtain the fractions of ice meltwater (f_i), snow meltwater (f_s) and rainwater (f_r) by random sampling of tracers of three sources ($\delta^{18}O_i$, d_i; $\delta^{18}O_s$, d_s, and $\delta^{18}O_r$, d_r) from a given range in which an essential condition is for every possible combination sample points fall within a triangle formed by three end-members. A random sampling of $\delta^{18}O$ and d values from the defined compositional range is justified because Table 2 shows that these values are equally probable in nature as supported by near-uniform distribution in Histogram plots (Figure S2 in Supporting Information S1). Monte Carlo simulation with 10,000 times iteration was used in MATLAB R2021b to calculate the fractional contribution of end-member water sources to the total discharge. The final fractions here are the mean of 10,000 iterations of Equations 4–6 (Boral et al., 2019). It is noteworthy to mention that the iterations were successfully executed only when the stream composition fell within the mixing space created by end-member values, thereby resulting only positive values. To convert the fractional end-member components into the volumetric flow, we multiplied the fractional components with the corresponding total discharge.

2.5.4. Separation of Monsoonal Rainfall Component Using Water Balance Method

We used a water balance approach to independently calculate rainwater contribution to the total discharge (Hasnain, 1999; Thayyen et al., 2005). Briefly, the surface runoff in the Mandakini River Basin was derived from the glacier-covered area (GCA) and glacier-free area (GFA) because rain falling over GCA is routed to proglacial

Table 2
Ranges of Isotopic Compositions of the End Members of Ice, Snow, and Rain (Season Specific and Event Specific)

End members	$\delta^{18}O$ (‰)			d (‰)		
	Mean	+20%	−20%	Mean	+20%	−20%
Ice	−14.61	−11.69	−17.53	15.08	18.1	12.07
Snow	−7.4	−5.92	−8.88	23.3	27.96	18.64
Rain_Pre-ISM	−5.52	−4.42	−6.62	11.19	13.43	8.95
Rain_Post-ISM	−15.81	−12.65	−18.97	27.11	32.53	21.69
Rain end member	Rain event	Mean	+5%	−5%	Mean	+5%	−5%
19-July-19	R1: 08-July (D)	−2.80	−2.66	−2.94	14.06	14.77	13.36
14-July-19	R2: 14-July (D)	−7.52	−7.14	−7.9	13.97	14.67	13.27
17-July-19	R3: 17-July (D)	−5.69	−5.41	−5.98	9.72	10.2	9.23
19-July-19	R4: 20-July (D)	−2.80	−2.66	−2.94	14.06	14.77	13.36
31-July-19	R5: 1-August (D)	−11.62	−11.04	−12.2	11.33	11.90	10.77
7-August-19	R6: 07-August (D)	−18.10	−17.20	−19.01	16.99	17.84	16.14
19-August-19	R7: 10-August (D)	−27.62	−26.24	−29.00	12.44	13.06	11.82
13-August-19	R8: 13-August (D)	−15.43	−14.66	−16.21	13.74	14.42	13.05
19-August-19	R9: 22-August (D)	−27.62	−26.24	−29.00	12.44	13.06	11.82
25-August-19	R10: 25-August (D)	−12.61	−11.98	−13.24	9.51	9.99	9.03
25-August-19	R11: 31-August (N)	−12.61	−11.98	−13.24	9.51	9.99	9.03

Note. Data sources: Ice data: Ahluwalia et al. (2016), Boral et al. (2019), and Rai et al. (2013) and this study; Snowfall data: Kumar et al. (2018); Rain data of Pre-M and Post-M: (Kumar et al., 2018); Event specific rain data: this study. For details information of ice end member see Table S1 in Supporting Information S2.

streams through the glacial drainage system without any major water loss, whereas rain falling over GFA is subjected to loss due to infiltration. The GCA and GFA of the glacier basin were estimated at 200 m intervals using shapefiles and DEMs (Digital Elevation model) of the whole glacier basin and glacier-covered area in ArcGIS 10.8. By subtracting the GCA from the whole basin area the GFA was calculated. The area–elevation distribution of the Chorabari Glacier is shown in Figure S3 in Supporting Information S1, and Table S2 in Supporting Information S2. We used a runoff coefficient of 0.7 for the GFA, based on earlier studies on Himalayas (Bookhagen & Burbank, 2010; Hasnain, 1999; Thayyen et al., 2005). The surface runoff generated from rainfall also depends on the aerial extent of respective zones that is, area under which precipitation occurs in the form of rainfall. In regions with high altitudes and glaciers, the type of precipitation changes from rainfall to snowfall with increasing altitude. The studied catchment ranges between 6,400 m a.m.s.l at the head to 3,895 m a.m.s.l at the sampling location, and we used 0°C as the rain-snow threshold temperature (Misra et al., 2020). The distribution of rainfall-affected areas in the catchment was calculated from daily mean air temperature data of the study period using the mean lapse rate for June-September 5.1°C km^{-1} (Misra et al., 2020). The area with air temperature higher than 0°C was considered as rainfall-affected regions. For each rainfall event, we divided the area below 0°C into intervals of 200 m in altitude and for each interval, we calculated the rainfall component at that elevation, considering the corresponding rain temperature obtained using the mean lapse rate and mean air temperature of corresponding rain events. The rainfall component was calculated from daily rainfall data measured near the snout using the following relationship:

$$\text{Runoff from total basin}: R_T = R_{\text{GCA}} + R_{\text{GFA}} \tag{13}$$

$$\text{For glacier} - \text{covered area}: R_{\text{GCA}} = P \times A_{\text{GCA}} \tag{14}$$

$$\text{and for glacier free area}: R_{\text{GFA}} = 0.7 \times P \times A_{\text{GFA}} \tag{15}$$

where R_T, R_{GCA}, and R_{GFA} are rainfall in m^3 s^{-1} derived surface runoff from total glacier basin, GCA, and GFA, respectively, P is the amount of total rainfall for each day in meter, A_{GCA} and A_{GFA} are area of glacier-covered
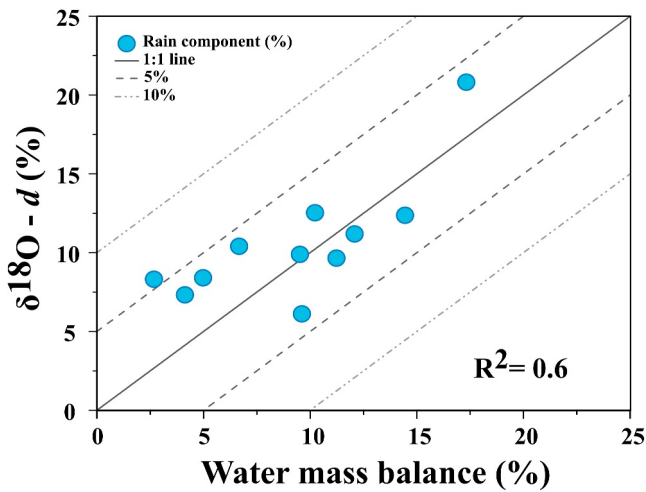
Figure 4. Comparison of rain components calculated using mixing model and water mass balance method. The solid line represents 1:1 line. Dashed lines represent 5% and 10% relative deviation from 1:1 line.

zone, and glacier free zone with air temperature >0°C in m^2. The fractional contributions of rainwater from water mass balance approach and δ^{18}O-d mixing model are in agreement. Result shows that the calculated fractions are within a 5% deviation from the 1:1 line (Figure 4 and Table S3 in Supporting Information S2).

3. Results

3.1. Hydrometeorological Data

Temporal variations of rainfall data and discharge data are shown in Figure 5. Gauging data shows the Chorabari Glacier received 665 mm of total rainfall from June through October. The glacier received 62, 129, 393, 63, and 18 mm of total rainfall in the months of June–October, respectively. The discharge at daytime and nighttime shows limited variability. In general, the discharge started increasing from the first week of July, peaked in August, and started to decline from the first week of September.

3.2. Temporal Variability of Oxygen and Hydrogen Isotopes

The variability of δ^{18}O and δD in ice, rainwater, and proglacial meltwater samples are plotted in Figure 2. The ice samples δ^{18}O compositions range between $-12.56‰$ and $-14.67‰$ (average: $-13.66 \pm 0.83‰$, $n = 6$, 1 S.D.) and δD compositions range between $-84.05‰$ and $-101.37‰$ (average: $-92.09 \pm 6.62‰$, $n = 6$, 1 S.D.). The rainwater samples show a large range in δ^{18}O and δD from highly depleted to enriched isotopic composition (Table S4 in Supporting Information S2). The δ^{18}O and δD compositions of rainwater ($n = 27$) fall close to the river water line (RWL) and the best fit local meteoric water line (LMWL) has a slope = 8.0 and deuterium intercept = 12.6‰ (Figure 2). The best fit RWL has a slope = 8.5 and deuterium intercept = 24.3‰ through all data points ($n = 78$) and is described by positive d values. The δ^{18}O and δD compositions of river water fall above the global meteoric water line (GWML; $\delta D = 8.17 \ \delta^{18}O + 11.27$; Rozanski et al., 2013). Our river water samples were compared with Kali Gandaki River—a well-studied river basin in the Central Himalayas—samples from Hassenruck-Gudipati et al. (2023) and both follow the similar trend clustering above the GMWL. Since the δ^{18}O and δD data from the Global Network of Isotopes in Rivers (GNIR) and the Global Network of Isotopes in Precipitation (GNIP) database closely follows the GMWL (Halder et al., 2015), and our database closely followed the GMWL, it is evident that evaporation has not altered the isotope composition of river water (Craig, 1961). The best-fit RWL for pre-monsoon, monsoon, and post-monsoon season has a slope of 8.1, 8.6, 6.9, respectively, and intercepts of 21.7‰, 25.4‰, 2.8‰, respectively, through all the data points for pre-monsoon ($n = 17$), monsoon ($n = 31$), and post-monsoon ($n = 30$) months. Seasonal and diurnal variations of δ^{18}O and δD of river water are shown using box plots (Figure 2). During the pre-monsoon season the isotopic composition of river water shows enrichment, as indicated by the higher values of δ^{18}O and δD. The isotopic composition becomes depleted with the progress of the ablation season. Furthermore, when considering the diurnal variations, daytime samples show higher isotopic values, indicating enrichment compared to nighttime samples. The statistical significance test with a significance level of $\alpha = 0.05$, shows that the diurnal variation is more pronounced in pre-monsoon indicating statistically significant differences in δ^{18}O and δD composition at a diurnal scale (δ^{18}O: $p = 0.03$; δD: $p = 0.01$). However, during the monsoon and post-monsoon seasons, there are no statistically significant differences between daytime and nighttime variations in stable water isotopes (δ^{18}O: $p = 0.1$ and δD: $p = 0.1$ for the monsoon; δ^{18}O: $p = 0.2$ and δD: $p = 0.1$ for post-monsoon).

3.3. Relationship of Discharge With Mean Air Temperature and Rainfall Amount

A correlation between daytime discharge and mean air temperature for each month was established and is reported in Table S5 in Supporting Information S2. Unfortunately, a correlation with nighttime discharge cannot be established due to the unavailability of the nighttime air temperature data. The correlation of discharge-mean air temperature with a time lag ($t = 0, 1, 2, 3$ days) for June revealed that there is a good correlation ($r = 0.5$, $p < 0.05$, $n = 27$) with mean air T with zero-time lag. However, the correlation reduced with an increasing time lag. In the monsoonal season (July–August), a negative correlation is observed, although not significant ($r = -0.1$, $p < 0.05$,
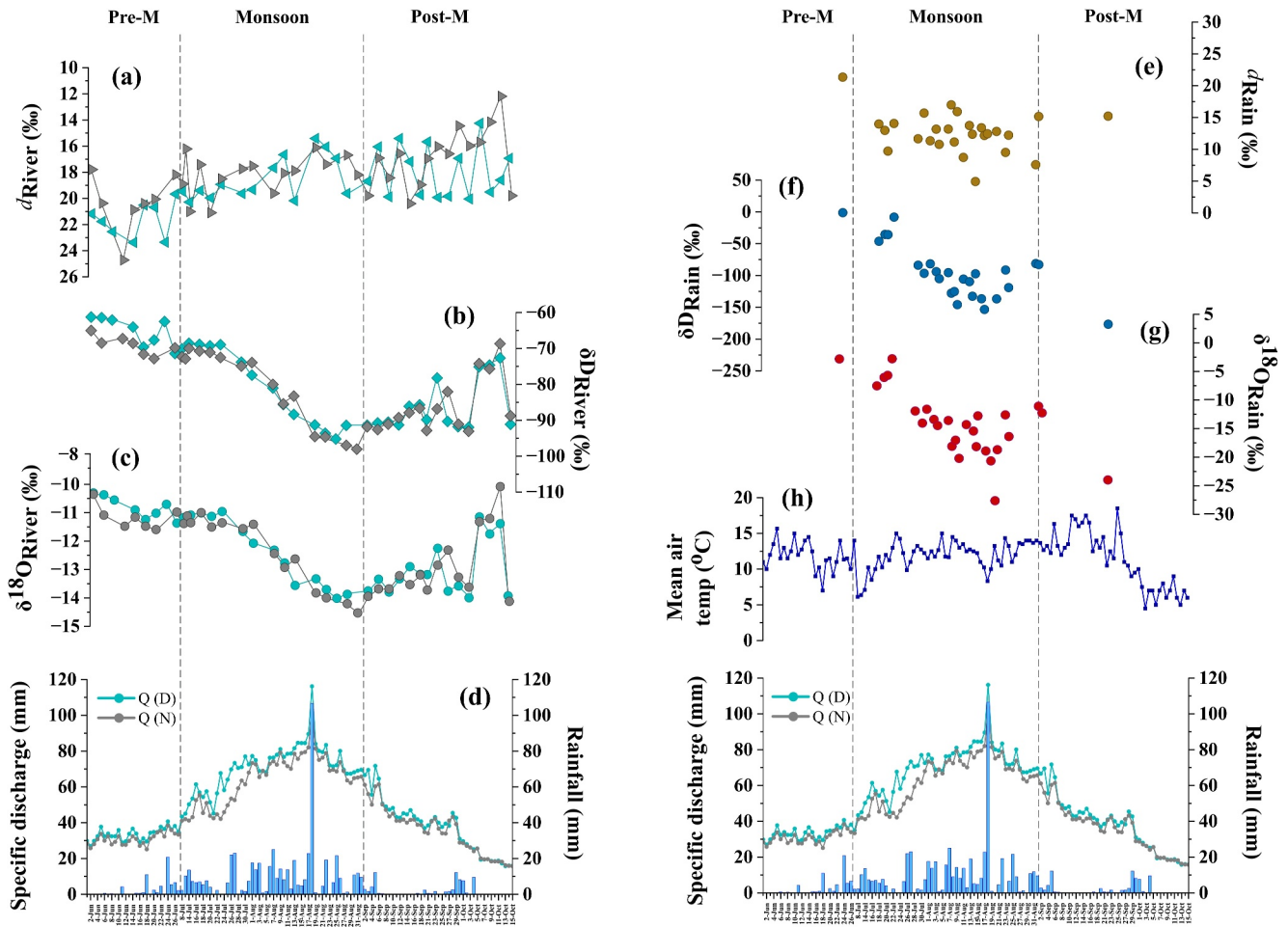
Figure 5. Time series trend of isotopic signatures of river water (a–c) and rainwater (e–g) with daily specific discharge and rainfall (d), and mean air temperature (h) for the ablation period of 2019. Variability of river water isotope data as well as discharge for daytime and nighttime is shown in bluish-green and gray color respectively.

$n = 48$). Individually, July is moderately correlated ($r = 0.4$, $p < 0.05$, $n = 17$) and August is strongly negatively correlated ($r = -0.7$, $p < 0.05$, $n = 31$) with the mean air temperature at zero-time lag. During the post-monsoon season (September- and mid-October), the correlation coefficient shows a strong positive correlation ($r = 0.7$, 0.8, 0.7, and 0.7, $p < 0.05$, $n = 42$) for all lag periods.

To demonstrate the influence of rainfall amount on meltwater discharge, the correlation coefficient between rainfall intensities and discharge was calculated and reported in Table S6 in Supporting Information S2. As June and October months experienced very little rainfall, the rainfall-discharge correlation for June and October months was not established. The discharge of August strongly correlates with rainfall ($r = 0.7$, $p < 0.05$, $n = 31$ for daytime; $r = 0.5$, $p < 0.05$, $n = 31$ for nighttime), whereas July does not show any significant correlations ($r = 0.2$, $p < 0.05$, $n = 17$ for daytime; 0.03, $p < 0.05$, $n = 17$ for nighttime). Rainfall with 0-day lag exhibits a better correlation with discharge compared to time lags. In general, the post-monsoon season (considering September and October months together) shows a poor correlation between rainfall and discharge ($r = 0.4$, $p < 0.05$, $n = 42$ for both daytime and nighttime) compared to the monsoonal season ($r = 0.6$, $p < 0.05$, $n = 48$ for daytime; $r = 0.5$, $p < 0.05$, $n = 48$, for nighttime) with zero-day lag.

3.4. Ice Meltwater, Snow Meltwater, and Rainwater Contributions to the Total Discharge Between Day to Night, Seasons, and During Major Rain Events

The relative fractions of ice meltwater, snow meltwater, and rainwater to the total discharge show substantial variability over diurnal and seasonal variability (Figure 6 and Table 1). For example, the daytime discharge during
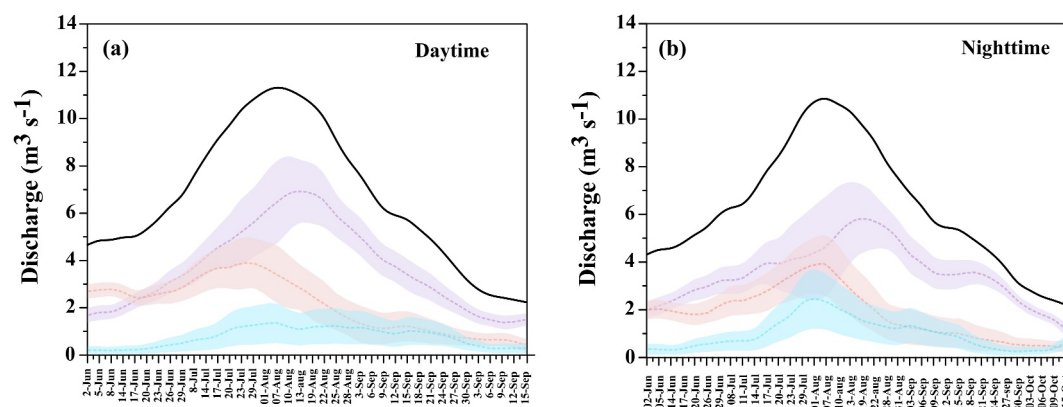
Figure 6. 5-point moving average plots of calculated volumetric flows of ice (purple), snow (light red) and rainwater (blue) in river water for (a) daytime and (b) nighttime discharge. Dashed lines are the average of the end member contribution and shaded regions represent ± one standard deviation of the results. Black line represents total meltwater discharge.

pre-monsoon (June) was dominated by snow meltwater contribution with $53.8 \pm 6.2\%$ (2.30 ± 0.27 m^3 s^{-1}, $n = 9$, 1 S.D.), followed by ice meltwater of $41.4 \pm 6.3\%$ (1.84 ± 0.27 m^3 s^{-1}, $n = 9$, 1 S.D.), and rainwater contribution is minimum with $4.8 \pm 3.5\%$ (0.21 ± 0.15 m^3 s^{-1}, $n = 9$, 1 S.D.) (Figure 6a; Table S7 in Supporting Information S2). At the onset of ISM in the month of July, the ice meltwater and snow meltwater contribution increased to $49.5 \pm 8.8\%$ (3.99 ± 0.71 m^3 s^{-1}, $n = 6$, 1 S.D.) and $42 \pm 9.4\%$ (3.35 ± 0.75 m^3 s^{-1}, $n = 6$, 1 S.D.), respectively, whereas the rainwater discharge increased by a factor of three (0.68 ± 0.46 m^3 or $8.5 \pm 5.7\%$, s^{-1}, $n = 6$, 1 S.D.). During the peak monsoon season, the ice meltwater and rainwater contribution increased up to $60.1 \pm 12.7\%$ (6.36 ± 1.47 m^3 s^{-1}, $n = 8$, 1 S.D.) and $10.7 \pm 6.7\%$ (1.24 ± 0.77 m^3 s^{-1}, $n = 8$, 1 S.D.), respectively, while, the snow meltwater contribution started to decline with contribution of $29.2 \pm 9\%$ (3.32 ± 1.04 m^3 s^{-1}, $n = 8$, 1 S.D.). In September and October, the stream discharge was dominantly controlled by ice meltwater runoff accounting for $63.3 \pm 11.2\%$ (4.12 ± 0.72 m^3 s^{-1}, $n = 10$, 1 S.D.) and $60.3 \pm 11.2\%$ (1.64 ± 0.32 m^3 s^{-1}, $n = 5$, 1 S.D.) respectively, of the total discharge. The daytime and nighttime hydrographs of ice meltwater, snow meltwater, and rainwater on a seasonal time scale did not show any significant variability (Table S7 in Supporting Information S2).

A notable daytime to nighttime variability in the contributions of ice meltwater, snow meltwater, and rainwater was observed (Table S7 in Supporting Information S2). For example, at the beginning of the melting season, ice meltwater contribution was in general higher in the stream during the nighttime with $49.7 \pm 7.8\%$ (2.22 ± 0.34 m^3 s^{-1}, $n = 7$, 1 S.D.) compared to the daytime ice meltwater contribution of $41.4 \pm 6.3\%$ (1.84 ± 0.27 m^3 s^{-1}, $n = 9$, 1 S.D.). Moreover, nighttime contribution is dominated by ice meltwater (Table S7 in Supporting Information S2). During the peak monsoon period in the month of August, ice meltwater flow during daytime was significantly higher showing $60.1 \pm 12.7\%$ (6.36 ± 1.47 m^3 s^{-1}, $n = 8$, 1 S.D.) of contribution in comparison to nighttime contribution of $45.77 \pm 17.7\%$ (4.79 ± 1.89 m^3 s^{-1}, $n = 8$, 1 S.D.), although the total discharge was similar (daytime average: 10.97 ± 1.3 m^3 s^{-1}, $n = 31$, 1 S.D.; nighttime: 10.37 ± 1.1 m^3 s^{-1}, $n = 31$, 1 S.D.). However, at the end of the melting season in the month of October, daytime and nighttime discharge were both dominated by ice meltwater with nighttime ice meltwater contribution higher ($68.1 \pm 9.3\%$ or 2.31 ± 0.23 m^3 s^{-1}, $n = 4$, 1 S.D.) than daytime (Table S7 in Supporting Information S2).

Hydrograph separation results after the major rainfall events (rainfall rate of a minimum of 2 mm d^{-1} and separated by dry period no longer than 4 hr) revealed contributions from all three source end members for corresponding rain events. The resulting ice component and rain component exhibited good autocorrelation, with a correlation coefficient (Pearson's r) value of 0.9 and 0.5 for 1-day lag value ($p < 0.05$, $n = 11$). Hence, we used Spearman's correlation to understand the relationship of rain intensity and all the three source end members. It is worth mentioning that we used Spearman's correlation due to high autocorrelation in the hydrological data, making the use of parametric statistics like Pearson's correlation coefficient impractical (Kundzewicz & Robson, 2004). The statistical test revealed two major observations (a) rainwater runoff to the total discharge correlated with rainfall intensity (Spearman's rho = 0.9, $p < 0.05$, $n = 11$) and (b) ice meltwater contribution shows a positive correlation with rainfall intensity (Spearman's rho = 0.6, $p < 0.05$, $n = 11$) (Figure 7). However,
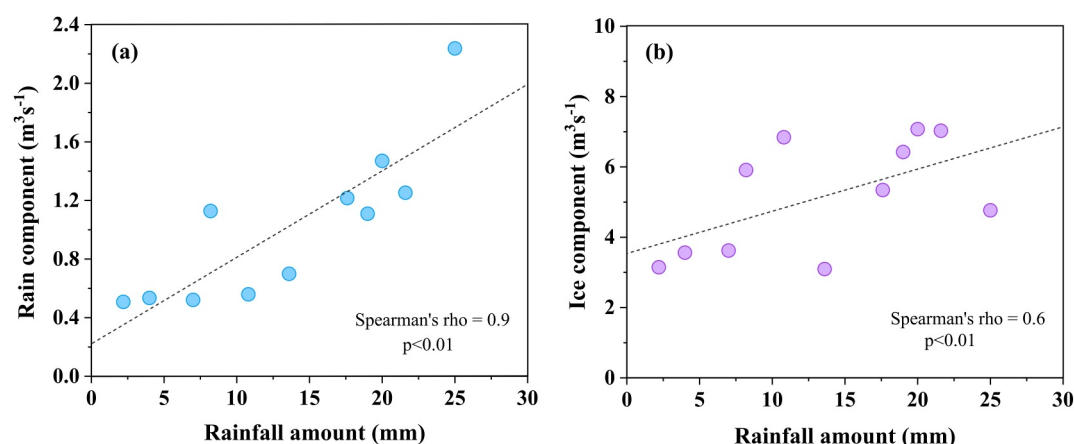
Figure 7. Correlation coefficients of rain amount with (a) rain component, and (b) ice component results from δ^{18}O-d model for 11 rainfall events. Here rain component and ice component indicate volumetric flows of rain contribution and ice contribution which were calculated by multiplying the contribution (%) with discharge of river.

snow meltwater runoff did not show any significant correlation with rainfall, with correlation coefficient (Spearman's rho) values of 0.1 ($p < 0.05$, $n = 11$) (Figure S4 in Supporting Information S1).

4. Discussion

Here we discuss the possible reasons for our key observations:

1. Air temperature and rainfall have complex control on the glacial hydrology.
2. The water source end-member contributions from ice meltwater, snow meltwater, and rainwater discharge in the stream shows diurnal and seasonal variability.
3. The rain event significantly altered the water source end-member contributions namely high ice meltwater contribution was observed during major rain events.

4.1. The Impact of Air Temperature and Rainfall on Seasonal Discharge

At the beginning of the melting season, discharge shows a better correlation with the mean air temperature (Table S5 in Supporting Information S2) because during the pre-monsoon season (a) the primary contribution to the river discharge originates from the melting of the fresh snowpacks and (b) there is a minimal contribution from rainfall. During the monsoonal period, the relationship of meltwater discharge with air temperature becomes more complex. The poor correlation between air temperature and discharge during the monsoonal season can be attributed to the intricate response mechanisms of discharge. This includes (a) the simultaneous contribution from both snow and ice meltwater as the melted snowpacks have exposed the ice surface, and (b) the notable influence of rainfall, which results in increased direct runoff. Further, snow and ice surface melt at different rates. During the monsoonal period, reduced insolation, and a rapid decline in the average albedo of the glacier surface due to the exposure of old dirty ice result in a higher ice melt rate compared to the pre-monsoonal period. Additionally, the lower and middle sections of the glacier—particularly in the ablation zone—are partially covered with debris (Dobhal et al., 2013) which leads to a distinct melt rate and uneven melting under specific temperature conditions across the glacier surface. Hence, the uneven melting conditions in the glacier, contributions from both snow and ice, and significant rainfall in the glacier basin lead to fluctuations in river flow resulting in reduced correlations between discharge and air temperature (Singh et al., 2000, 2006). The analysis of the discharge–air temperature correlation during the post-monsoonal period reveals a higher correlation compared to that of the monsoonal period (Table S5 in Supporting Information S2), indicating the influence of air temperature on river discharge. During post-monsoon season, a substantial portion of the glacier ice is exposed due to the depletion of the snow cover by September. This exposure facilitates a more immediate impact of meltwater generated over the glacier surface (Singh et al., 2000). However, discharge generated during this period is comparatively lower than that of the monsoonal period. This is attributed to the decrease in temperature from September onwards, resulting in reduced melting of snow and ice. Furthermore, the lower amount of rainwater contribution leads to reduced

fluctuation in river discharge. Thus, the systematic recession of flow due to weaker melting conditions and minimal contribution to river flow from rainfall may be the contributing factors for a strong correlation for the post-monsoon season.

Correlations between discharge and rainfall exhibit notable strength during the monsoonal period compared to the post-monsoon period (Table S6 in Supporting Information S2). Specifically, August demonstrates a very strong correlation, and the river flow displays a quicker response to rainfall in August compared to other months. This variation can be attributed to changes in the physical conditions of the glacier. During this period, that is, in August, a substantial portion of the glacier ice surface is exposed (Misra et al., 2020). The response to rainfall is faster from an ice-covered surface compared to a snow-covered one. Rainfall on a snow-covered surface is initially absorbed by the snowpack and released later into the river discharge. However, the impervious nature of the ice surface allows rain to contribute to the runoff at the outlet in a relatively shorter time period (Singh et al., 2006), Further, the drainage network within the glacier is well established which enables the meltwater and rainwater to reach the basin outlet more rapidly. As a result, the lag time of the runoff generated from rainfall over the ice surface is less than that for rain over the snow surface (Singh et al., 2000). Moreover, a pronounced correlation with zero-time lag compared to other time lag suggests a quicker response to river flow to rainfall in August. There is also a distinction between daytime and nighttime correlations, with substantial contribution to streamflow occurring at the corresponding time lag (Singh et al., 2000, 2006). The notable decrease in correlation coefficients for the post-monsoonal period can be attributed to various factors, including (a) the occurrence of precipitation as rainfall in the lower part of the glacier basin and as snowfall in the upper reaches, (b) the influence of the melting-freezing process, which contributes to the delaying effect as the weather begins to colder (Singh et al., 2000).

4.2. Causes of Diurnal and Seasonal Variability of Ice Meltwater, Snow Meltwater, and Rainwater Contribution to the Total Discharge

The seasonal variability of ice meltwater, snow meltwater, and rainwater depends on many factors such as the variability in the snow-covered area, incoming solar radiation, degree of debris cover, and rainfall intensity (Alexander et al., 2011; Hock, 2005; Reznichenko et al., 2010; Scherler et al., 2011; Singh et al., 2006, 2011). Figure 5f shows that discharge starts to increase from June, reaches its maximum in July and August, and then again starts to decline. At the beginning of the glacier ablation season, increased river discharge represents the initiation of the glacier melting process. In the early part of the melting season, the snowpack starts melting as evidenced by the changes in the snow cover areas in the Himalayas (Misra et al., 2020). As the melting season progresses, in general, the snow cover starts disappearing exposing the ice surface to direct melting. In the monsoon season, ice meltwater discharge dominates, and snow meltwater is mostly derived from high-elevation regions. As expected, a significant contribution from rainwater to the stream discharge was observed during the monsoon season. As the melting season migrates from monsoon to a cooler and drier post-monsoon season, overall meltwater generation slowly decreases as evident in the lower discharge (Figure 5d). We would like to mention that the streamflow in the post-monsoon season is dominated by the ice meltwater discharge as during post-monsoon the ice surface is the most exposed due to minimal snow cover. This glacier melting process aligns with the snow cover data over the glacier (Misra et al., 2020). Satellite images of the Chorabari glacier reveal no substantial changes in the snow cover area above the Equilibrium Line Altitude (ELA: 5,500 m a.s.l.). This observation implies that precipitation primarily occurs in the form of snowfall at higher elevations. Additionally, there is no accumulation below 5,500 m a.s.l. during the ablation season signifying a continuous depletion of snow cover area throughout the ablation season.

The diurnal variability of ice meltwater, snow meltwater, and rainwater contribution to the total discharge can be attributed to various factors namely weather condition, the surface state of glacier (whether snow covered or snow and firn free), and physiographical features of the basin (Singh et al., 2006). Diurnal variation in source contribution is mostly observed in pre and post monsoonal periods. This variation offer crucial insights into the hydrological responses including drainage and storage characteristics, as well as in the delayed runoff from the basin (Jansson et al., 2003; Lecce, 1993; Mingjie et al., 2013; M. Tranter & Raiswell, 1991). Table S7 in Supporting Information S2 shows, during pre-monsoon season (June month), daytime discharge is dominated by snow meltwater whereas nighttime discharge is dominated by ice melt water. At the onset of the ablation season, basin exhibits robust storage characteristics. During this period, significant melting of extensive snow cover across the entire ablation area occurs at daytime whereas at night, the absence of solar radiation prevents glacier

melting process. However, snow meltwater generated during the day is, in part, retained in the basin and subsequently released (Benn et al., 2017; Miles et al., 2020; Singh et al., 2006). As this released meltwater flows subglacially or englacially (Singh et al., 2006), it induces further internal melting of ice (Alexander et al., 2011). Additionally, the basal melting of ice, driven by geothermal and frictional heat flux, further contributes to the generation of ice meltwater (Alexander et al., 2011). In post-monsoon period, significant melting of glacier ice occurs as a considerable portion of glacier ice surface becomes exposed due to the depletion of snow cover (Singh et al., 2000). At the end of ablation season, during October month, the higher contribution of ice at nighttime can be attributed to the fluctuation of the available energy in melting as well as storage characteristics of the basin. Limited melting occurs during the daytime, primarily due to a decrease in air temperature toward the end of the ablation season. However, the observed runoff at night indicates the release of water already stored in accumulation area (Singh et al., 2006). This stored water may further contribute to ice melting through the heat advection process. Furthermore, the transfer of heat from the debris layer can be an additional factor for nighttime ice melting. A study by Reznichenko et al. (2010), revealed that ice melted most rapidly under a 10 mm debris cover, and the melting rate decreases as debris thickness exceeded 5 cm. This suggests that the presence of debris reduces melt rate but doesn't always serve as a complete insulator. Surface ablation rate in Chorabari glacier reaches its maximum of around 2.3–3.3 m yr^{-1} where debris cover is relatively thin (∼2 cm at altitude around 4,400–4,500 m a.s.l.) (Dobhal et al., 2013). It is plausible that during daytime, the surface with thin debris cover absorbs heat, and the accumulated heat is gradually released at nighttime, potentially causing the melting of ice beneath the debris cover (Östrem, 1959).

4.3. Impact of Rain Events on Water Source End-Members' Flow Dynamics

Results from δ^{18}O-d mixing model for identified 11 rainfall events show that during rainfall events, not only rainwater contribution but also the ice meltwater contribution to the total discharge increases. Figure 7 shows a positive correlation between ice meltwater and rainfall amount, with a resulting correlation coefficient (Spearman's rho) value of 0.6 ($p < 0.01$, $n = 11$). This runs contrary to conventional thinking that higher rainwater contribution to the streamflow will dilute the ice meltwater fractions (relative contributions) as intense rainfall contributes to increased direct runoff while a reduction in incoming solar radiation due to cloudy skies leads to less meltwater production. However, we observed that the higher ice meltwater contribution to the total discharge increases during rainfall events. The correlation between snow meltwater and rainwater discharge is generally poor, with correlation coefficient (Spearman's rho) values of 0.1 ($p < 0.01$, $n = 11$) (Figure S4 in Supporting Information S1). This is not a surprise as rainfall events only happened during the monsoon months, which had minimal snow cover.

The overall higher discharge during the monsoonal period along with an increased ice meltwater contribution during rainfall events in River Mandakini can be attributed to various processes. These processes include (a) the release of stored meltwater due to the reorganization of the englacial and subglacial drainage network during rainfall events (Ahmad & Hasnain, 2001; Bartholomew et al., 2011; Benn et al., 2017; Miles et al., 2019). A good positive correlation between rainfall amount and discharge during the monsoonal months for zero-time lag suggests a quick response of runoff to rainfall caused due to well-established drainage systems in glaciers (Singh et al., 2000). The supply of more water during heavy rainfall events increases the hydraulic pressure on englacial and subglacial channels, thus more channels open and transport stored meltwater more effectively during the monsoonal season (Das et al., 2008; Engel et al., 2016; Van de Griend & Arwert, 1983). (b) It is also possible that rain heat flux where rain falls over the glacier surface increases the near-surface temperature by releasing sensible and latent heat. The release of latent heat of fusion due to refreezing causes the heating and melting of the ice surface. The meltwater produced at the surface, or rain water, percolates downward and refreezes upon contact with ice that still maintains a negative temperature (June & Hock, 2010). For debris-covered glaciers ice, rain percolates through the debris layer and enhances the melting rate of ice lying beneath debris (Reznichenko et al., 2010; Sakai et al., 2004). The observed poor correlation between discharge and air temperature during the monsoon season suggests that monsoonal discharge is not solely controlled by the radiation-induced generation of glacier meltwater.

We assessed the impact of fallen rainfall on glacier surface using an energy balance calculation, using the equations outlined in Keegan et al. (2014) (Doyle et al., 2015; Hock, 2005; Konya & Matsumoto, 2010). We briefly outline the parameters used in the calculations for the 11 rainfall events in our study. The sensible heat flux

releasing from rain falling over ice surface that is at the freezing point ($T_i = 0°C$), can be calculated by using the equation:

$$Q_{R_{0c}} = Q_{RS} = \rho_w C_w R(T_r - T_i) \tag{16}$$

Where $Q_{R_{0c}}$ is the heat flux by rain when surface temperature of ice is 0°C, Q_{RS} is the sensible heat flux by rain, ρ_w is density of water (1,000 kg m^{-3}), C_w is specific heat of water (4.182 kJ kg^{-1} K^{-1}), R is the rainfall amount, T_r is temperature of rainfall and T_i is surface temperature of glacier ice (0°C). The amount of rainfall and rain temperature for the 11 rainfall events are given in Table S8 in Supporting Information S2. The latent heat flux released by rain through englacial cooling and freezing, can be calculated as:

$$Q_{RH} = \rho_w \lambda_w R \tag{17}$$

Where Q_{RH} is the latent heat flux, λ_w is latent heat of fusion (334 kJ kg^{-1}). The sensible and latent heat combines to give the total energy flux of rain when it falls over ice or snow surface that is below freezing point ($T_i < 0°C$):

$$Q_{R\_2C} = \rho_w C_w R(T_r - T_i) + \rho_w \lambda_w R \tag{18}$$

Where Q_{R_2C} is the total energy flux released by rainfall falling over ice surface that is at <0°C.

The energy flux by rainfall Q_R, will induce glacier melting through three distinct phases: (a) Warming phase (Q_{cc}) in which energy is required to raise the temperature to an isothermal temperature 0°C, (b) ripening phase (Q_{m2}), in which absorbed energy is required to melt but meltwater still retain in snowpack or within ice matrix, and (c) output phase (Q_{m3}), in which further absorption of energy results in the generation of meltwater that drains from the snowpack or ice structure (Dingman, 2015; Keegan et al., 2014). Hence, the total energy (Q_M) required to melt and generate meltwater output is:

$$Q_M = Q_{cc} + Q_{m2} + Q_{m3}$$

$$Q_M = -c_i \rho_w h_m (T_i - T_m) + \Theta_{ret} h_i \rho_w \lambda_f + (h_m - h_{wret}) \rho_w \lambda_f \tag{19}$$

Where C_i is the specific heat capacity of ice (2.102 kJ kg^{-1} K^{-1}), ρ_w is the density of water (1,000 kg m^{-3}), h_m is the water equivalent in snowpack or glacier ice (meters), T_i is temperature of glacier ice, T_m is the melting temperature (273 K), Θ_{ret} is the maximum volumetric water content, h_i is the depth of ice depth (meters), λ_f is latent heat of fusion (334 kJ kg^{-1}), and h_{wret} is the liquid water retaining capacity of snowpack or glacier ice (meters). The h_{wret} can be calculated as, $h_{wret} = \Theta_{ret} h_i$ (Dingman, 2015; Hock, 2005; Kegan et al., 2014). Assuming energy released by rain through englacial cooling and freezing is used for glacier ice melting then, $Q_R = Q_M$. Subsequently, either Equation 19 combined with Equation 16 or Equation 18 can be solved to calculate meltwater equivalent, h_m when rain falls over glacier surface (T_i) at 0°C and −2°C (Table S8 in Supporting Information S2).

Rain-induced heat flux calculation showed that melt generated due to rain-induced heat mainly depends on rainfall intensity (for ice surface at 0°C, Pearson's $r = 0.98$, $p < 0.01$ and for ice surface at −2°C, Pearson's $r = 0.95$, $p < 0.01$) (Figure S5 in Supporting Information S1). We found that events R4 and R9 that is, 4 and 20 mm rainfall of 10°C falling over exposed ice surface at 0°C can generate 0.23 and 1.14 m^3 s^{-1} surface melt of ice, which are 3.15% and 9.69% of the total discharge, respectively (Table S8 in Supporting Information S2). When rainfall occurs over ice surface at −2°C, it can generate ice melt of 0.3 and 1.47 m^3 s^{-1}, which are ~4.05% and 12.49% of total discharge, respectively (Boral et al., 2019; Doyle et al., 2015). Therefore, rain heat flux calculations reveal that rain events over ice surfaces can enhance ice melt rates as observed in our isotope-mixing model results (Table S8 in Supporting Information S2). Our results suggest that rainfall events can enhance ice meltwater discharge near the snout point of glacier-fed Himalayan rivers, and rain-induced melting of glaciers can work in tandem with reorganization of the englacial and subglacial drainage network.

5. Future Scope

We emphasize that this research is ongoing and needs more data across several years and several catchments. Firstly, more work is required to underpin the $\delta^{18}O$ and $d/\delta D$ compositions of end-members that is, ice meltwater, snow meltwater, and rainfall. Quantifying the end-member composition is a challenging task as the $\delta^{18}O$ and $d/\delta D$ composition of ice meltwater, snow meltwater, and rainfall will show natural variability in space and time controlled by a complex association of time, altitude, moisture source, rainfall amount, and others (Jeelani et al., 2010; Kumar et al., 2010; Rai et al., 2009). Moreover, the kinetic fractionation between snow/ice and meltwater will make the river water more depleted in the heavier isotopes and become similar to the lighter ice samples (Feng et al., 2002; Taylor et al., 2001). Therefore, it is often difficult to delineate the contributions from glaciers and precipitation using only environmental tracers such as $\delta^{18}O$ and d. To overcome these limitations, we did not use unique the $\delta^{18}O$ and $d/\delta D$ values in our hydrograph separation model and used ranges. In future, $\delta^{18}O$ and $d/\delta D$ variability of ice cores and catchment scale precipitation data sets should be used, which are so far missing.

Further, our knowledge about the impact of rainfall on the ice and snow mass stored is still in its "infancy." For example, in addition to "rain-induced glacier melting," the percentage of rainfall that drains directly through the crevasses and moulins to enhance the subglacial, englacial, and supraglacial drainage network to transport surge of meltwater in streams and the fraction of rain that would be converted to surface runoff and flow in supraglacial lakes or englacial conduits is still an open question. The glaring lack of ground observation data that can quantify the role of rainfall on glacial hydrology severely limits the accuracy and predictive power of hydrologic models in glacierized catchments. Such data would not only help to better understand the effects of climate change on the hydrological regimes of glacier-fed rivers under the influence of the Indian monsoon but would also help to better quantify the magnitude of water catastrophes associated with heavy rainfall in glacierized basins.

Apart from the direct impact of rain droplets on enhanced meltwater runoff, rain-bearing warm moisture-saturated winds can overcast the glacierized basins further melting the glaciers beyond the rain events (Bennartz et al., 2013; Hanna et al., 2014; Oltmanns et al., 2019). Moreover, winter rain can quickly freeze, and these shiny layers possess more heat-absorbing capacity in comparison to fresh snowflakes. When exposed to a higher temperature, a snowpack with multiples of these frozen snow layers is subject to early onset of melting (Fox, 2019). Therefore, the impact of changing rainfall patterns on ice and snow surface would not only impact the surface mass balance of the glaciers and meltwater runoff but would also impact glacial processes such as snow metamorphism, ice flow dynamics such as short-term acceleration in ice speed flow (Doyle et al., 2015; Niwano et al., 2021; Singh et al., 1997), and weathering rates. Further, extreme rainfall can act as the principal driver of glacier lake outburst floods (GLOF) triggered by the failure of moraine dams, ice calving, and slope failure which are all well-established (Mir et al., 2018; Musselman et al., 2018; Shangguan et al., 2017; Shukla & Sen, 2021; Worni et al., 2012). Moreover, seasonal evaluation of the subglacial drainage system of valley glacier has significant implication for subglacial biogeochemistry and the composition of microbial communities (Hodson et al., 2008; Nienow et al., 1998; Tranter et al., 2005). The transition from anoxic to oxic/suboxic conditions in channel margin zones, along with increased drainage efficiency and reduced rock: water ratios, impact microbial activity, solute fluxes and dissolution of silicate minerals which may affect the downstream ecosystem. This study only attempted to constrain the role of rainfall in ice melting, all the above-mentioned questions still need to be addressed to fully determine the role of changing rainfall patterns in glacial hydrology and their effects on downstream ecosystems in the context of cryospheric research.

6. Conclusion

A tracer-based ($\delta^{18}O$ and d) three-component mixing model was used to quantify the relative fractions of ice meltwater, snow meltwater, and rainwater to the total discharge across the entire ablation season of 2019 in River Mandakini, Upper Ganga Basin. The mixing model result reveals that the water source end-members show significant variability, both in the diurnal and seasonal time scales. Results indicate that snow meltwater dominates the pre-monsoon season, whereas, in monsoon, the discharge is predominantly controlled by rainwater. In the post-monsoon season, ice meltwater is the dominant water source end-member in the stream because the snow cover area was minimum. The study also reveals a positive correlation between rainwater and ice meltwater discharge in the river during major rain events. The increase of ice meltwater flow in the river during major rain events on the glacier indicates that rainfall triggers the enhancement of ice meltwater contribution to the total

discharge. We conclude that rainfall events on glaciers can be an additional driver of the increment of ice meltwater discharge in the glacier-fed streams.

Conflict of Interest

The authors declare no conflicts of interest relevant to this study.

Data Availability Statement

Calculations related to water balance method and rain-induced meltwater are published in Figshare Repository at https://doi.org/10.6084/m9.figshare.25785204.v3 (Roy et al., 2024).

References

Ahluwalia, R. S., Rai, S. P., Gupta, A. K., Dobhal, D. P., Tiwari, R. K., Garg, P. K., & Kesharwani, K. (2016). Towards the understanding of the flash flood through isotope approach in Kedarnath valley in June 2013, Central Himalaya, India. *Natural Hazards*, *82*(1), 321–332. https://doi.org/10.1007/s11069-016-2203-6

Ahmad, S., & Hasnain, S. I. (2001). Snow and stream-water chemistry of the Ganga headwater basin, Garhwal Himalaya, India. *Hydrological Sciences Journal*, *46*(1), 103–111. https://doi.org/10.1080/02626660109492803

Alexander, D., Shulmeister, J., & Davies, T. (2011). High basal melting rates within high-precipitation temperate glaciers. *Journal of Glaciology*, *57*(205), 789–795. https://doi.org/10.3189/002214311798043726

Banerjee, A., Dimri, A. P., & Kumar, K. (2020). Rainfall over the Himalayan foot-hill region: Present and future. *Journal of Earth System Science*, *129*, 1–16. https://doi.org/10.1007/s12040-019-1295-2

Barros, A. P., Joshi, M., Putkonen, J., & Burbank, D. W. (2000). A study of 1999 monsoon rainfall in a mountainous region in central Nepal using TRMM products and rain gauge observations. *Geophysical Research Letters*, *27*(22), 3683–3686. https://doi.org/10.1029/2000GL011827

Bartholomew, I., Nienow, P., Sole, A., Mair, D., Cowton, T., Palmer, S., & Wadham, J. (2011). Supraglacial forcing of subglacial drainage in the ablation zone of the Greenland ice sheet. *Geophysical Research Letters*, *38*(8). https://doi.org/10.1029/2011gl047063

Benn, D. I., Bolch, T., Hands, K., Gulley, J., Luckman, A., Nicholson, L. I., et al. (2012). Response of debris-covered glaciers in the Mount Everest region to recent warming, and implications for outburst flood hazards. *Earth-Science Reviews*, *114*(1–2), 156–174. https://doi.org/10.1016/j.earscirev.2012.03.008

Benn, D. I., Thompson, S., Gulley, J., Mertes, J., Luckman, A., & Nicholson, L. (2017). Structure and evolution of the drainage system of a Himalayan debris-covered glacier, and its relationship with patterns of mass loss. *The Cryosphere*, *11*(5), 2247–2264. https://doi.org/10.5194/tc-11-2247-2017

Bennartz, R., Shupe, M. D., Turner, D. D., Walden, V. P., Steffen, K., Cox, C. J., et al. (2013). July 2012 Greenland melt extent enhanced by low-level liquid clouds. *Nature*, *496*(7443), 83–86. https://doi.org/10.1038/nature12002

Bhutiyani, M. R. (2000). Sediment load characteristics of a proglacial stream of Siachen Glacier and the erosion rate in Nubra valley in the Karakoram Himalayas, India. *Journal of Hydrology*, *227*(1–4), 84–92. https://doi.org/10.1016/s0022-1694(99)00174-2

Bookhagen, B., & Burbank, D. W. (2010). Toward a complete Himalayan hydrological budget: Spatiotemporal distribution of snowmelt and rainfall and their impact on river discharge. *Journal of Geophysical Research*, *115*(3), 1–25. https://doi.org/10.1029/2009JF001426

Boral, S., & Sen, I. S. (2020). Tracing "Third Pole" ice meltwater contribution to the Himalayan rivers using oxygen and hydrogen isotopes. *Geochemical Perspectives Letters*, *13*, 48–53. https://doi.org/10.7185/geochemlet.2013

Boral, S., Sen, I. S., Ghosal, D., Peucker-Ehrenbrink, B., & Hemingway, J. D. (2019). Stable water isotope modeling reveals spatio-temporal variability of glacier meltwater contributions to Ganges River headwaters. *Journal of Hydrology*, *577*(July), 123983. https://doi.org/10.1016/j.jhydrol.2019.123983

Brunello, C. F., Andermann, C., Marc, O., Schneider, K. A., Comiti, F., Achleitner, S., & Hovius, N. (2020). Annually resolved monsoon onset and withdrawal dates across the Himalayas derived from local precipitation statistics. *Geophysical Research Letters*, *47*(23), e2020GL088420. https://doi.org/10.1029/2020gl088420

Clark, I. (2015). Groundwater geochemistry and isotopes. *Groundwater Geochemistry and Isotopes*. https://doi.org/10.1201/b18347

Craig, H. (1961). Isotopic variations in meteoric waters. *Science*, *133*(3465), 1702–1703. https://doi.org/10.1126/science.133.3465.1702

Dansgaard, W. (1964). Stable isotopes in precipitation. *Tellus*, *16*(4), 436–468. https://doi.org/10.3402/tellusa.v16i4.8993

Das, S. B., Joughin, I., Behn, M. D., Howat, I. M., King, M. A., Lizarralde, D., & Bhatia, M. P. (2008). Fracture propagation to the base of the Greenland Ice Sheet during supraglacial lake drainage. *Science*, *320*(5877), 778–781. https://doi.org/10.1126/science.1153360

Dingman, S. L. (2015). *Physical hydrology* (3rd ed.). Waveland press.

Dobhal, D. P., Mehta, M., & Srivastava, D. (2013). Influence of debris cover on terminus retreat and mass changes of Chorabari Glacier, Garhwal region, central Himalaya, India. *Journal of Glaciology*, *59*(217), 961–971. https://doi.org/10.3189/2013JoG12J180

Doyle, S. H., Hubbard, A., Van De Wal, R. S. W., Box, J. E., Van As, D., Scharrer, K., et al. (2015). Amplified melt and flow of the Greenland ice sheet driven by late-summer cyclonic rainfall. *Nature Geoscience*, *8*(8), 647–653. https://doi.org/10.1038/ngeo2482

Engel, M., Penna, D., Bertoldi, G., Agnese, A. D., Soulsby, C., & Comiti, F. (2016). Identifying run-off contributions during melt-induced run-off events in a glacierized alpine catchment. *Hydrological Processes*, *364*(3), 343–364. https://doi.org/10.1002/hyp.10577

Feng, X., Taylor, S., Renshaw, C. E., & Kirchner, J. W. (2002). Isotopic evolution of snowmelt 1. A physically based one-dimensional model. *Water Resources Research*, *38*(10), 35-1–35-8. https://doi.org/10.1029/2001wr000814

Fox, A. (2019). Rain is melting Greenland's ice, even in winter, raising fears about sea level rise. *Science*. https://doi.org/10.1126/science.aax2520

Frenierre, J. L., & Mark, B. G. (2014). A review of methods for estimating the contribution of glacial meltwater to total watershed discharge. *Progress in Physical Geography*, *38*(2), 173–200. https://doi.org/10.1177/0309133313516161

Halder, J., Terzer, S., Wassenaar, L. I., Araguás-Araguás, L. J., & Aggarwal, P. K. (2015). The Global Network of Isotopes in Rivers (GNIR): Integration of water isotopes in watershed observation and riverine research. *Hydrology and Earth System Sciences*, *19*(8), 3419–3431. https://doi.org/10.5194/hess-19-3419-2015

Han, T., Zhang, M., Wang, S., Qu, D., & Du, Q. (2020). Sub-hourly variability of stable isotopes in precipitation in the marginal zone of East Asian monsoon. *Water (Switzerland)*, *12*(8), 2145. https://doi.org/10.3390/W12082145

Hanna, E., Fettweis, X., Mernild, S. H., Cappelen, J., Ribergaard, M. H., Shuman, C. A., et al. (2014). Atmospheric and oceanic climate forcing of the exceptional Greenland ice sheet surface melt in summer 2012. *International Journal of Climatology*, *34*(4), 1022–1037. https://doi.org/10.1002/joc.3743

Hasnain, S. I. (1999). Runoff characteristics of a glacierized catchment, Garhwal Himalaya, India. *Hydrological Sciences Journal*, *44*(6), 847–854. https://doi.org/10.1080/02626669909492284

Hassenruck-Gudipati, H. J., Andermann, C., Dee, S., Brunello, C. F., Baidya, K. P., Sachse, D., et al. (2023). Moisture sources and pathways determine stable isotope signature of Himalayan waters in Nepal. *AGU Advances*, *4*(1), e2022AV000735. https://doi.org/10.1029/2022av000735

Heim, A., & Gansser, A. (1939). In *Central Himalaya: Geological observations of the Swiss expedition, 1936* (Vol. 73). Hindustan Publishing Corporation.

Hock, R. (2005). Glacier melt: A review of processes and their modelling. *Progress in Physical Geography*, *29*(3), 362–391. https://doi.org/10.1191/0309133305pp453ra

Hock, R., Rasul, G., Adler, C., Cáceres, B., Gruber, S., Hirabayashi, Y., et al. (2019). High mountain areas. In H.-O. Pörtner, D. C. Roberts, V. Masson-Delmotte, P. Zhai, M. Tignor, E. Poloczanska, et al. (Eds.), *IPCC special report on the ocean and cryosphere in a changing climate* (pp. 131–202).

Hodson, A., Anesio, A. M., Tranter, M., Fountain, A., Osborn, M., Priscu, J., et al. (2008). Glacial ecosystems. *Ecological Monographs*, *78*(1), 41–67. https://doi.org/10.1890/07-0187.1

Immerzeel, W. W., Van Beek, L. P. H., & Bierkens, M. F. P. (2010). Climate change will affect the Asian water towers. *Science*, *328*(5984), 1382–1385. https://doi.org/10.1126/science.1183188

Jansson, P., Hock, R., & Schneider, T. (2003). The concept of glacier storage. *Review*, *282*(1–4), 116–129. https://doi.org/10.1016/S0022-1694(03)00258-0

Jeelani, G. H., Bhat, N. A., & Shivanna, K. (2010). Use of δ18O tracer to identify stream and spring origins of a mountainous catchment: A case study from Liddar watershed, western Himalaya, India. *Journal of Hydrology*, *393*(3–4), 257–264. https://doi.org/10.1016/j.jhydrol.2010.08.021

Jones, J. N., Boulton, S. J., Stokes, M., Bennett, G. L., & Whitworth, M. R. (2021). 30-year record of Himalaya mass-wasting reveals landscape perturbations by extreme events. *Nature Communications*, *12*(1), 6701. https://doi.org/10.1038/s41467-021-26964-8

June, F. M., & Hock, R. (2010). Glacier meteorology energy balance. *Energy*, 1–10.

Karakoti, I., Kesarwani, K., Mehta, M., & Dobhal, D. P. (2017). Modelling of meteorological parameters for the Chorabari Glacier valley, central Himalaya, India. *Current Science*, *112*(07), 1553–1560. https://doi.org/10.18520/cs/v112/i07/1553-1560

Katzenberger, A., Schewe, J., Pongratz, J., & Levermann, A. (2021). Robust increase of Indian monsoon rainfall and its variability under future warming in CMIP6 models. *Earth System Dynamics*, *12*(2), 367–386. https://doi.org/10.5194/esd-12-367-2021

Keegan, K. M., Albert, M. R., McConnell, J. R., & Baker, I. (2014). Climate change and forest fires synergistically drive widespread melt events of the Greenland Ice Sheet. *Proceedings of the National Academy of Sciences of the United States of America*, *111*(22), 7964–7967. https://doi.org/10.1073/pnas.1405397111

Klaus, J., & McDonnell, J. J. (2013). Hydrograph separation using stable isotopes: Review and evaluation. *Journal of Hydrology*, *505*, 47–64. https://doi.org/10.1016/j.jhydrol.2013.09.006

Konya, K., & Matsumoto, T. (2010). Influence of weather conditions and spatial variability on glacier surface melt in Chilean Patagonia. *Theoretical and Applied Climatology*, *102*(1), 139–149. https://doi.org/10.1007/s00704-009-0248-0

Kraaijenbrink, P. D. A., Bierkens, M. F. P., Lutz, A. F., & Immerzeel, W. W. (2017). Impact of a global temperature rise of 1.5 degrees Celsius on Asia's glaciers. *Nature*, *549*(7671), 257–260. https://doi.org/10.1038/nature23878

Kumar, A., Gokhale, A. A., Shukla, T., & Dobhal, D. P. (2016). Hydroclimatic influence on particle size distribution of suspended sediments evacuated from debris-covered Chorabari Glacier, upper Mandakini catchment, central Himalaya. *Geomorphology*, *265*, 45–67. https://doi.org/10.1016/j.geomorph.2016.04.019

Kumar, A., Tiwari, S. K., Verma, A., & Gupta, A. K. (2018). Tracing isotopic signatures (δD and δ^{18}O) in precipitation and glacier melt over Chorabari Glacier–Hydroclimatic inferences for the Upper Ganga Basin (UGB), Garhwal Himalaya. *Journal of Hydrology: Regional Studies*, *15*, 68–89. https://doi.org/10.1016/j.ejrh.2017.11.009

Kumar, A., Verma, A., Dobhal, D. P., Mehta, M., & Kesarwani, K. (2014). Climatic control on extreme sediment transfer from Dokriani Glacier during monsoon, Garhwal Himalaya (India). *Journal of Earth System Science*, *123*(1), 109–120. https://doi.org/10.1007/s12040-013-0375-y

Kumar, B., Rai, S. P., Kumar, U. S., Verma, S. K., Garg, P., Kumar, S. V., et al. (2010). Isotopic characteristics of Indian precipitation. *Water Resources Research*, *46*(12). https://doi.org/10.1029/2009wr008532

Kumar, N., Ramanathan, A., Arora, A., Soheb, M., Mandal, A., Sharma, P., & Ranjan, S. (2020). Study of isotopic seasonality to assess the water source of proglacial stream in Chhota Shigri Glaciated Basin, Western Himalaya. *Hydrological Processes*, *34*(5), 1285–1300. https://doi.org/10.1002/hyp.13676

Kundzewicz, Z. W., & Robson, A. J. (2004). Change detection in hydrological records—A review of the methodology. *Hydrological Sciences Journal*, *49*(1), 7–19. https://doi.org/10.1623/hysj.49.1.7.53993

Lecce, S. A. (1993). Flow separation and diurnal variability in the hydrology of Conness Glacier, Sierra Nevada, California, USA. *Journal of Glaciology*, *39*(132), 216–222. https://doi.org/10.1017/S0022143000015872

Lee, J., Feng, X., Faiia, A. M., Posmentier, E. S., Kirchner, J. W., Osterhuber, R., & Taylor, S. (2010). Isotopic evolution of a seasonal snowcover and its melt by isotopic exchange between liquid water and ice. *Chemical Geology*, *270*(1–4), 126–134. https://doi.org/10.1016/j.chemgeo.2009.11.011

Mark, B. G., & Mckenzie, J. M. (2007). Tracing increasing tropical Andean glacier melt with stable isotopes in water. *Environmental Science and Technology*, *41*(20), 6955–6960. https://doi.org/10.1021/es071099d

Maurer, J. M., Schaefer, J. M., Rupper, S., & Corley, A. (2019). Acceleration of ice loss across the Himalayas over the past 40 years. *Science Advances*, *5*(6). https://doi.org/10.1126/sciadv.aav7266

Maurya, A. S., Shah, M., Deshpande, R. D., Bhardwaj, R. M., Prasad, A., & Gupta, S. K. (2011). Hydrograph separation and precipitation source identification using stable water isotopes and conductivity: River Ganga at Himalayan foothills. *Hydrological Processes*, *25*(10), 1521–1530. https://doi.org/10.1002/hyp.7912

Miles, E. S., Steiner, J., Willis, I., Buri, P., Immerzeel, W. W., Chesnokova, A., & Pellicciotti, F. (2017). Pond dynamics and supraglacial-englacial connectivity on debris-covered Lirung Glacier, Nepal. *Frontiers in Earth Science*, *5*, 69. https://doi.org/10.3389/feart.2017.00069

Miles, E. S., Willis, I. C., Arnold, N. S., Steiner, J., & Pellicciotti, F. (2017). Spatial, seasonal and interannual variability of supraglacial ponds in the Langtang Valley of Nepal, 1999–2013. *Journal of Glaciology*, *63*(237), 88–105. https://doi.org/10.1017/jog.2016.120

Miles, K. E., Hubbard, B., Irvine-Fynn, T. D., Miles, E. S., Quincey, D. J., & Rowan, A. V. (2020). Hydrology of debris-covered glaciers in High Mountain Asia. *Earth-Science Reviews*, *207*, 103212. https://doi.org/10.1016/j.earscirev.2020.103212

Miles, K. E., Hubbard, B., Quincey, D. J., Miles, E. S., Irvine-Fynn, T. D. L., & Rowan, A. V. (2019). Surface and subsurface hydrology of debris-covered Khumbu Glacier, Nepal, revealed by dye tracing. *Earth and Planetary Science Letters*, *513*, 176–186. https://doi.org/10.1016/j.epsl.2019.02.020

Mingjie, G., Tianding, H., Baisheng, Y., & Keqin, J. (2013). Characteristics of melt water discharge in the Glacier No. 1 basin, headwater of Urumqi River. *Journal of Hydrology*, *489*(1), 180–188. https://doi.org/10.1016/j.jhydrol.2013.03.013

Mir, R. A., Jain, S. K., Lohani, A. K., & Saraf, A. K. (2018). Glacier recession and glacial lake outburst flood studies in Zanskar basin, western Himalaya. *Journal of Hydrology*, *564*, 376–396. https://doi.org/10.1016/j.jhydrol.2018.05.031

Misra, A., Kumar, A., Bhambri, R., Haritashya, U. K., Verma, A., Dobhal, D. P., et al. (2020). Topographic and climatic influence on seasonal snow cover: Implications for the hydrology of ungauged Himalayan basins, India. *Journal of Hydrology*, *585*, 124716. https://doi.org/10.1016/j.jhydrol.2020.124716

Musselman, K. N., Lehner, F., Ikeda, K., Clark, M. P., Prein, A. F., Liu, C., et al. (2018). Projected increases and shifts in rain-on-snow flood risk over western North America. *Nature Climate Change*, *8*(9), 808–812. https://doi.org/10.1038/s41558-018-0236-4

Nienow, P., Sharp, M., & Willis, I. (1998). Seasonal changes in the morphology of the subglacial drainage system, Haut Glacier d'Arolla, Switzerland. *Earth Surface Processes and Landforms: The Journal of the British Geomorphological Group*, *23*(9), 825–843. https://doi.org/10.1002/(sici)1096-9837(199809)23:9<825::aid-esp893>3.0.co;2-2

Niwano, M., Box, J. E., Wehrlé, A., Vandecrux, B., Colgan, W. T., & Cappelen, J. (2021). Rainfall on the Greenland ice sheet: Present-day climatology from a high-resolution non-hydrostatic polar regional climate model. *Geophysical Research Letters*, *48*(15), e2021GL092942. https://doi.org/10.1029/2021gl092942

Oltmanns, M., Straneo, F., & Tedesco, M. (2019). Increased Greenland melt triggered by large-scale, year-round cyclonic moisture intrusions. *The Cryosphere*, *13*(3), 815–825. https://doi.org/10.5194/tc-13-815-2019

Östrem, G. (1959). Ice melting under a thin layer of moraine, and the existence of ice cores in moraine ridges. *Geografiska Annaler*, *41*(4), 228–230. https://doi.org/10.1080/20014422.1959.11907953

Østrem, G. (1964). A method of measuring water discharge in turbulent streams. *Geographical Branch, Department of Mines and Technical Surveys*. https://doi.org/10.4095/331213

Panicker, A. S., Sandeep, K., Gautam, A. S., Gandhi, N., Beig, G., Nainwal, H. C., et al. (2019). Chemical composition and isotopic signatures of ice and snow over a Himalayan Glacier (Satopanth) in India. *SN Applied Sciences*, *1*(10), 1–7. https://doi.org/10.1007/s42452-019-0966-6

Penna, D., & van Meerveld, H. J. I. (2019). Spatial variability in the isotopic composition of water in small catchments and its effect on hydrograph separation. *Water*, *6*(5), 1–33. https://doi.org/10.1002/wat2.1367

Phillips, D. L., & Gregg, J. W. (2003). Source partitioning using stable isotopes: Coping with too many sources. *Oecologia*, *136*(2), 261–269. https://doi.org/10.1007/s00442-003-1218-3

Pu, T., Wang, K., Kong, Y., Shi, X., Kang, S., Huang, Y., et al. (2020). Observing and modeling the isotopic evolution of snow meltwater on the southeastern Tibetan Plateau. *Water Resources Research*, *56*(9), e2019WR026423. https://doi.org/10.1029/2019wr026423

Rai, S. P., Kumar, B., Arora, M., & Singh, R. D. (2013). Isotopic characterization of snow, ice and glacial melt in the western Himalayas, India.

Rai, S. P., Kumar, B., & Singh, P. (2009). Estimation of contribution of southwest monsoon rain to Bhagirathi River near Gaumukh, western Himalayas, India, using oxygen-18 isotope. *Current Science*, *97*(2), 240–245.

Rai, S. P., Singh, D., Jacob, N., Rawat, Y. S., Arora, M., & Bhishm, K. (2019). Identifying contribution of snowmelt and glacier melt to the Bhagirathi River (Upper Ganga) near snout of the Gangotri Glacier using environmental isotopes. *Catena*, *173*, 339–351. https://doi.org/10.1016/j.catena.2018.10.031

Reznichenko, N., Davies, T., Shulmeister, J., & McSaveney, M. (2010). Effects of debris on ice-surface melting rates: An experimental study. *Journal of Glaciology*, *56*(197), 384–394. https://doi.org/10.3189/002214310792447725

Roy, N., & Sen, I. S. (2023). CO_2 consumption rates in the glacierized Himalayan headwaters: The importance of sulfuric and nitric acid-mediated chemical weathering reactions in geologic carbon cycle. *Geochemistry, Geophysics, Geosystems*, *24*(7), e2023GC010919. https://doi.org/10.1029/2023gc010919

Roy, N., Sen, I. S., Boral, S., Shukla, T., & Velu, V. (2024). Isotope hydrograph separation reveals rainfall on the glaciers will enhance ice meltwater discharge to the Himalayan rivers [Dataset]. *Figshare*. https://doi.org/10.6084/m9.figshare.25785204.v3

Rozanski, K., Araguás-Araguás, L., & Gonfiantini, R. (2013). Isotopic patterns in modern global precipitation (pp. 1–36). https://doi.org/10.1029/gm078p0001

Sakai, A., Fujita, K., & Kubota, J. (2004). Evaporation and percolation effect on melting at debris-covered Lirung Glacier, Nepal Himalayas, 1996. *Bulletin of Glacier Research*, *21*, 9–15.

Sangewar, C. V., Shukla, S. P., & Singh, R. K. (2009). Inventory of the Himalayan glaciers.

Scherler, D., Bookhagen, B., & Strecker, M. R. (2011). Spatially variable response of Himalayan glaciers to climate change affected by debris cover. *Nature Geoscience*, *4*(3), 156–159. https://doi.org/10.1038/ngeo1068

Shangguan, D., Ding, Y., Liu, S., Xie, Z., Pieczonka, T., Xu, J., & Moldobekov, B. (2017). Quick release of internal water storage in a glacier leads to underestimation of the hazard potential of glacial lake outburst floods from Lake Merzbacher in Central Tian Shan Mountains. *Geophysical Research Letters*, *44*(19), 9786–9795. https://doi.org/10.1002/2017GL074443

Sharmila, S., Joseph, S., Sahai, A. K., Abhilash, S., & Chattopadhyay, R. (2015). Future projection of Indian summer monsoon variability under climate change scenario: An assessment from CMIP5 climate models. *Global and Planetary Change*, *124*, 62–78. https://doi.org/10.1016/j.gloplacha.2014.11.004

Shekhar, M. S., Chand, H., Kumar, S., Srinivasan, K., & Ganju, A. (2010). Climate-change studies in the western Himalaya. *Annals of Glaciology*, *51*(54), 105–112. https://doi.org/10.3189/172756410791386508

Shukla, T., & Sen, I. S. (2021). Preparing for floods on the third pole. *Science*, *372*(6539), 232–234. https://doi.org/10.1126/science.abh3558

Singh, A. T., Rahaman, W., Sharma, P., Laluraj, C. M., Patel, L. K., Pratap, B., et al. (2019). Moisture sources for precipitation and hydrograph components of the Sutri Dhaka Glacier basin, western Himalayas. *Water (Switzerland)*, *11*(11), 2242. https://doi.org/10.3390/w11112242

Singh, P., Haritashya, U. K., Kumar, N., & Singh, Y. (2006). Hydrological characteristics of the Gangotri Glacier, central Himalayas, India. *Journal of Hydrology*, *327*(1–2), 55–67. https://doi.org/10.1016/j.jhydrol.2005.11.060

Singh, P., Kumar, A., & Kishore, N. (2011). Meltwater storage and delaying characteristics of Gangotri Glacier (Indian Himalayas) during ablation season. *Hydrological Processes*, *25*(2), 159–166. https://doi.org/10.1002/hyp.7828

Singh, P., Ramasastri, K. S., Kumar, N., & Arora, M. (2000). Correlations between discharge and meteorological parameters and runoff forecasting from a highly glacierized Himalayan basin. *Hydrological Sciences Journal*, *45*(5), 637–652. https://doi.org/10.1080/02626660009492368

Singh, P., Spitzbart, G., Hübl, H., & Weinmeister, H. W. (1997). Hydrological response of snowpack under rain-on-snow events: A field study. *Journal of Hydrology*, *202*(1–4), 1–20. https://doi.org/10.1016/S0022-1694(97)00004-8

Taylor, S., Feng, X., Kirchner, J. W., Osterhuber, R., Klaue, B., & Renshaw, C. E. (2001). Isotopic evolution of a seasonal snowpack and its melt. *Water Resources Research*, *37*(3), 759–769. https://doi.org/10.1029/2000wr900341

Thayyen, R. J., Gergan, J. T., & Dobhal, D. P. (2005). Monsoonal control on glacier discharge and hydrograph characteristics, a case study of Dokriani Glacier, Garhwal Himalaya, India. *Journal of Hydrology*, *306*(1–4), 37–49. https://doi.org/10.1016/j.jhydrol.2004.08.034

Tranter, M., & Raiswell, R. (1991). The composition of the englacial and subglacial component in bulk meltwaters draining the Gornergletscher, Switzerland. *Journal of Glaciology*, *37*(125), 59–66. https://doi.org/10.1017/S0022143000042805

Tranter, M., Skidmore, M., & Wadham, J. (2005). Hydrological controls on microbial communities in subglacial environments. *Hydrological Processes*, *19*(4), 995–998. https://doi.org/10.1002/hyp.5854

Turner, A. G., & Slingo, J. M. (2009). Subseasonal extremes of precipitation and active-break cycles of the Indian summer monsoon in a climate-change scenario. *Quarterly Journal of the Royal Meteorological Society: A Journal of the Atmospheric Sciences, Applied Meteorology and Physical Oceanography*, *135*(640), 549–567. https://doi.org/10.1002/qj.401

Van de Griend, A. A., & Arwert, J. A. (1983). The mechanism of runoff generation from an alpine glacier during a storm traced by oxygen $^{18}O^{16}O$. *Journal of Hydrology*, *62*(1–4), 263–278. https://doi.org/10.1016/0022-1694(83)90106-3

Wang, D., Tian, L., Cai, Z., Shao, L., Guo, X., Tian, R., et al. (2020). Indian monsoon precipitation isotopes linked with high level cloud cover at local and regional scales. *Earth and Planetary Science Letters*, *529*, 115837. https://doi.org/10.1016/j.epsl.2019.115837

Worni, R., Stoffel, M., Huggel, C., Volz, C., Casteller, A., & Luckman, B. (2012). Analysis and dynamic modeling of a moraine failure and glacier lake outburst flood at Ventisquero Negro, Patagonian Andes (Argentina). *Journal of Hydrology*, *444–445*, 134–145. https://doi.org/10.1016/j.jhydrol.2012.04.013